7/25/68

COMBINED HEAT AND VAPOR TRANSPORT MECHANISMS IN A POROUS IMPREGNATED CERAMIC

A THESIS

Presented to

The Faculty of the Graduate Division

By

Jerry Russell Dunn

In Partial Fulfillment

of the Requirements for the Degree

Doctor of Philosophy

in the School of Mechanical Engineering

Georgia Institute of Technology

December, 1972

COMBINED HEAT AND VAPOR TRANSPORT

MECHANISMS IN A POROUS IMPREGNATED CERAMIC

Approved:

Chairman

Date approved by Chairman 11/22/72

ACKNOWLEDGMENTS

The author wishes to express his sincere appreciation to his advisor, Dr. Charles W. Gorton, for his advice, encouragement and direction throughout this investigation. Special thanks are also expressed to Dr. P. Durbetaki, Dr. Henderson C. Ward, Dr. S. V. Shelton, and Dr. G. T. Colwell for their service on the reading and examining committees.

The assistance of Mr. Joseph Doyal and Mr. Lewis Cavalli in assembling the test facility was greatly appreciated. The author is also grateful to the School of Mechanical Engineering for the use of its equipment during the investigation.

The dedication and personal interest of the many instructors who have contributed to the author's education are appreciated.

Finally the author would like to express his deepest gratitude to his wife and family for their patience, understanding and encouragement during the period of this investigation.

TABLE OF CONTENTS

Chapter | Page

LIST OF TABLES

LIST OF ILLUSTRATIONS

Figure | Page

NOMENCLATURE

Symbol	
a_i	constants in enthalpy curve fits
A	constant in Appendix B
B	Blowing parameter
B_1	constant in Appendix B
C	specific heat
D_{12}	binary diffusion coefficient
E	constant in Appendix B
f'	non-dimensional velocity
F	constant in Appendix B
g	non-dimensional enthalpy
G	constant in Appendix B
h_i	enthalpy of species "i"
h_t	enthalpy of vaporized gases
Δh_v	effective heat of vaporization
I	stagnation enthalpy
k	thermal conductivity
k_p	equilibrium constant
L	slab thickness
Le	Lewis number
$\dot{m}$	convective mass flow rate per unit area
M_i	molecular weight of species "i"
n_i	total mass flux of species "i"

Symbol	
P	pressure
Pr	Prandtl number
q	heat transfer per unit area per unit time
Q	total heat transfer per unit area
r	radius in cylindrical coordinates
R_i	species gas constant
$r_{i;k}$	ratio by mass of element k in species "i"
s	body surface coordinate parallel to surface
$\overline{s}$	transformation variable
Sc	Schmidt number
T	temperature
T*	non-dimensional temperature in viscosity formulation
u	fluid velocity in main flow direction
U	non-dimensional velocity, equation 3.47, page 44
v	fluid velocity in cross flow direction
V_v	interface velocity
$\mathring{w}_i$	chemical generation rate per unit volume
w	variable defined by equation B.3a, page 113
x	coordinate in slab, normal to surface
x_i	species mole fraction
y	boundary layer coordinate, normal to slab
Y_i	species mass fraction
$\overline{Y}_k$	mass fraction of element k
z	jet coordinate defined in Figure 4, page 42
Z_i	non-dimensional mass fraction

Symbol	
$\overline{T}$, $\overline{X}$, $\overline{\tau}$	non-dimensional variables, equation 3.12, page 23

Subscripts

d	properties of solid matrix
e	free stream values
f	value for fuel in jet
i	component "i"
j	value at torch exit
o	initial condition of slab
p	properties in void space of slab
r	reference property values
R	denotes radiation
s	surface value in slab
v	value at interface
w	surface value in gas environment
1	effective values in region I
2	effective values in region II

Superscripts

+	terms evaluated on the positive side of a given position
-	terms evaluated on the negative side of a given position
'	denotes coordinates in moving reference frame

Greek Symbols

α	thermal diffusivity

<u>Symbol</u>

β	coefficient in equation 3.30, page 34
ϵ	parameter in Lennard-Jones potential
η	transformation variable
K	Boltzmann's constant
Λ	general transport parameter
π_{AB}, π_T	non-dimensional variables, equations 3.29, page 34
μ	viscosity
ρ	density
σ	porosity
σ_i	force constant in Lennard-Jones potential
τ	time
ϕ_K	defined by equation 3.29, page 34
$\phi_{i,K}$	viscosity parameter defined by equation C.5, page 120
$\Omega_i^{(2,2)*}$	non-dimensional collision cross-section

SUMMARY

The primary objective of this investigation was to develop an analysis for the thermal response of a porous, transpiration cooled, thermal protection material which included the thermal and chemical coupling phenomena of the test environment and to compare these results with experimental measurements.

A theory was developed for the transient temperature history of a porous ceramic, impregnated with a gelatine hydrate, subjected to the exhaust of an oxy-acetylene torch. The analysis considered the transient recession of the vaporizing impregnate interface and the resultant flow of water vapor through the porous matrix to the heated surface. Heat and vapor flow were assumed to be one dimensional in the direction normal to the heated surface with variable thermal conductivity and vapor specific heat on the heated side of the interface. The boundary condition at the heated surface included the effects of surface injection on the boundary layer profiles and included surface radiation and diffusion of gaseous species to and from the surface for thermal equilibrium among six chemical species: H_2O, CO_2, O_2, CO, H_2 and N_2.

A separate analysis was performed to determine the free stream chemistry and thermal properties along the axis of a turbulent, reacting jet considering mixing with a quiescent atmosphere. The results of this analysis provided the specification of the free stream thermal and chemical environment in the oxy-acetylene test facility. The

turbulent Lewis number was assumed to be unity and local thermodynamic equilibrium was assumed to exist in the jet.

The centerline stagnation pressure and heat transfer rate were measured for a range of fuel flow rates in the oxy-acetylene torch. Heating of the porous, impregnated samples was performed at a distance of 2.5 inches from the torch tip at a cold-wall heat flux of 150 BTU/ ft^2sec. The transient temperature response in the heated samples was monitored by thermocouples imbedded at depths from .125 to 1.0 inch below the heated surface.

The results of the turbulent mixing analysis indicated a significant variation in element mass fraction along the axis of the jet as a result of mixing with the atmosphere. This indicated that the environmental chemistry to which a given sample was exposed was dependent upon the location in the jet exhaust.

Surface recombination was affected by the depletion of available oxygen as the torch tip was approached. The net effect of surface chemistry in the energy balance at the heated surface predicted a positive contribution to the net surface heat transfer as a result of surface recombination.

Tests of the porous impregnated samples indicated that approximately 700 seconds were required for the gelatine interface to recede through the matrix. A definite isothermal period was indicated with the passage of the interface past a given point.

A calculation of the total energy transmitted to the porous matrix, indicated approximately 50 percent went into stored energy of the gases released with impregnate vaporization and approximately

20 percent went to interface vaporization. The analysis predicted that at locations closer to the torch tip, the contribution of surface chemistry to the heat transfer and the contribution of the impregnate vapor to the thermal protection increased.

An analysis of the system response in an air environment at the same cold-wall heat flux and free stream temperature indicated minimal difference in the protection time. However the relative contribution of surface recombination, surface injection, and hot-wall effects were significantly different.

CHAPTER I

INTRODUCTION

The analysis, testing, and evaluation of structural and thermal protection materials is a common task in engineering. This task has been significantly complicated, however, by advanced space flight requirements and other severe thermal environments such as the "3000 R" gas turbine (1)*. With the wide range of test durations, temperature levels, flow dynamics, and environmental chemistry of these applications, it is no longer sufficient to select materials on just the ability to withstand a given environmental temperature. Advanced protection systems, utilizing ablation or transpiration cooling, have introduced new phenomenological considerations and protection criteria in their many applications. A second difficulty arises through experimental evaluation procedures common to high temperature material testing. Many tests are not made under conditions simulating the application environment. If the data analysis techniques do not include the significant environmental coupling phenomena, evaluation of experimental results for application in other environments become uncertain and perhaps even arbitrary. Even with the inclusion of significant coupling phenomena, the problem of estimating their respective contributions under other than known test conditions is often difficult.

* Numbers in parentheses refer to cited references, page 125.

The problem considered herein provides an analysis of one thermal protection material with a parallel effort to couple the analysis to the actual experimental conditions such that criteria for evaluation in other environments can be established. Emphasis was placed on the mechanism of environmental interactions and the relative contributions of various phenomena relative to the total thermal protection. The analysis and experimental tests considered a transpiration cooled porous ceramic with a hydrous impregnate; however, the basic method and phenomena considered apply to a broad range of transpiration cooled systems.

The system proposed for study is a porous ceramic, slip cast fused silica foam (SCFS), impregnated with commerical unflavored gelatine containing water of hydration. This system incorporates several of the best characteristics of both the ablative and transpiration cooled systems. A comparatively low thermal conductivity material minimizes conduction into the interior. This also results in a rapid initial rise in surface temperature which reduces the free stream to surface temperature difference and increases radiation from the surface. Release of the vaporized impregnate (as discussed in the subsequent model) decreases the surface heat transfer due to the "blowing" effect. A further energy absorption occurs at the impregnate interface due to the hydrate vaporization. One advantage of this system is that dehydration and vaporization of the impregnate is self-regulating with respect to incident heat flux and does not require a coolant transfer system common to many transpiration cooling concepts.

Experimental testing was performed using a subsonic, oxygen-acetylene torch facility. The analysis points out the significant coupling phenomena associated with this environment and their importance in the evaluation of experimental results. While the results presented in this investigation apply directly to the transient response of an impregnated, porous ceramic in a particular environment, the basic methods developed for consideration of the phenomena involved in the analysis apply to either transient or steady-state conditions, with or without internal phase changes for a wide range of environmental chemistries.

CHAPTER II

HISTORICAL BACKGROUND

Literature related to the problem of interest here generally falls into the catagories of analyses of the thermal response of porous media and the effects of surface mass injection on boundary layer heat transfer.

Early analyses by Weinbaum and Wheeler (2), Schneider and Brogan (3), and Mendelsohn (4) considered the steady flow of a fluid through porous media. Weinbaum and Wheeler determined the steady-state temperature distribution whereas the latter two reports analyzed the transient thermal response assuming the surface heat flux was fixed or known through the surface heat transfer coefficient and basically, considered only the additional convective term in the energy equation for the temperature distribution in the porous matrix.

Grosh (5) performed an analytical study of a porous, liquid-filled media considering internal phase change at a moving interface. A similiar solution was obtained by assuming the interface position, x_V* , was directly proportional to $\sqrt{\tau}$. The results were completely uncoupled from the environment, however, by assuming a step change in surface temperature and thus eliminating the effects of surface reactions, mass addition, and boundary layer chemistry.

Studies of ablative systems (6, 7, 8, 9) generally centered on the prediction of the rate of ablative mass loss for various models

---

* The list of symbols is given on page xii

of aerodynamic heating. Bethe and Adams (7) considered the steady-state, stagnation point ablation of glassy materials. Reduction of surface heat transfer due to chemical reactions and surface radiation were not considered. It is pointed out in the discussion by Bethe and Adams that desirable properties of the ablative material include high heat capacity, high heat of vaporization and low thermal conductivity. They also note that the reduction in surface heat flux due to boundary layer injection decreases with increasing molecular weight of injectants.

Hidalgo (8) extended the analysis of Bethe and Adams to predict ablation away from the stagnation point for bodies of revolution. Results are presented for the respective contribution of vaporization, mass injection, radiation, and heat capacity to the total heat flux reduction. Vaporization accounts for approximately 60 percent of the energy transfer with the remainder somewhat evenly divided between the other phenomena. While the results are for steady-state ablation, the respective contributions are fairly constant for calculations made at two successive points along a trajectory. The proportionately high contribution by vaporization to the total energy absorbed is due in part to the high apparent latent heat of silica and the fact that the interface vaporization occurs at the heated surface. This is not the case for a porous, impregnated ceramic.

Koh and del Casal (9) analyzed the steady-flow of two fluids, NH_3 and air, through a porous matrix for fixed values of surface temperature and coolant reservoir temperature. In each case the effect of dissociation of the transpiring fluid was to significantly reduce the flow rate required to maintain a given surface temperature.

Important experimental studies include those of Poulos, Walton, and Elkins (10) and Gorton (11). The former performed initial tests on the feasibility of hydrated protection systems using a cement filled, stainless steel honeycomb structure and a porous ceramic filled with silica gel. Hydrate degradation contributed approximately 100 seconds to the total thermal protection of the cement system; however severe melting occurred in some tests. In similar results for the hydrous gel-filled ceramic, the impregnate was liberated without damage to the porous matrix. The time required for a specified backside temperature rise appeared to be from two to five times greater than that of unimpregnated samples. Advantages of the gel-filled system over that of the cement filled system include the fact that the gel-filled does not depend on the hydrate bond for its strength and that water contents of up to 50 percent by weight are possible. The study by Gorton (11) was concerned with the use of ammonia as a reactive coolant in steady flow through an electrically heated, porous, nichrome plate. Of particular importance was the estimation of the amount of energy attributed to internal NH_3 dissociation. The energy absorption due to ammonia dissociation was as much as 65 percent of the total energy absorption for a porous plate with a known internal, electrical heat generation. Likewise, the steady-state temperature gradient through the plate was significantly reduced with increased coolant flow for a given rate of heat generation.

Studies concerning the effects of mass injection on surface heat transfer are generally concerned with predicting the degree of surface heat flux reduction for various types and ranges of injection.

As such, the analyses are generally uncoupled from the transient body heating problem by considering either specified injection rates, fixed wall temperature, or both.

Lees (12) presented an analysis of convective heating considering boundary layer reactions with surface injection. An extension of this theory presented by Penner and Williams (13) resulted in the formulation of similar solutions for element mass fraction and stagnation enthalpy for Le = 1 that were independent of the chemical reaction model. Lees concluded that dissociation of the injected material would reduce heat transfer except for cases where catalytic recombination occurs at the surface.

The steady, cold-wall injection of helium was studied by Fox and Libby (14). Fair agreement is obtained with a previous conclusion by Georgeiv, et al. (15) that the surface heat transfer with foreign gas injection into air is proportional to the ratio of the molecular weight of air divided by that of the injectant.

Weston (16) considered air injection into the high speed, air boundary layer for fixed, cold-wall temperatures and steady-state conditions. Significantly higher heating rates are obtained considering equilibrium, real-air as compared to a previous perfect gas, linear viscosity versus temperature model. A subsequent analysis by Weston (17) considers steady N_2 injection from an ablating, porous carbon surface into a frozen boundary layer with chemical equilibrium at the surface. The nitrogen injection was found to significantly reduce carbon mass loss and also result in an order of magnitude lower heat flux at a blowing parameter of four as compared to the pure ablating case. One effect of wall chemistry was observed in an increase in wall enthalpy from 284 to 731 BTU/lbm at a fixed wall temperature of 2000°K when the N_2 injection rate was varied. This was attributed to the shift of element and therefore species concentration at the surface with mass addition.

A contrasting effect of surface mass addition on heat transfer was obtained by Scala and Gilbert (18) for the sublimation of graphite at hypersonic speeds. Oxidation of graphite to CO_2 and CO results in a positive contribution to the surface heat transfer. However, the blowing effect tends to decrease q_s with the net result that the heating level remains fairly constant. This analysis is again not coupled to the transient body response to the surface heating.

The results of the last two analyses justifies the statement by Penner and Libby (19) to the effect that the formulation of the non-steady ablation problem is strongly dependent upon the physico-chemical character of the ablating species.

Applications for a thermal protection system incorporating transpiration cooling can be seen in several areas of research. Of primary importance in the design formulation of the space shuttle is the concept of reusability. Faget (20) indicates that this criteria alone could lead to a cost per pound of pay load reduction of from one to two orders of magnitude. Thus an ablative type heat shield, with the resulting degradation of the surface covering would not be desirable. It is also indicated that surface temperatures under 2000 F are possible over 90 percent of the body. However, the duration of the total heat pulse could be up to 35 minutes depending on angle of attack during re-entry. A reusable porous matrix utilizing vaporization of a transpiration coolant could possibly provide the needed thermal protection at low surface temperatures and offer continued service.

A second application is seen in the trend to the high temperature gas turbine. Bayley and Turner (21) studied the application of transpiration cooling to both the turbine blades and combustion chamber with the results attractive in both cases. Theoretical studies indicate cooling air requirements to be reduced by factors of two to four compared with conventional film-cooling methods. The application to turbine blades would appear to make possible gas temperatures on the order of $1800^{\circ}K$. Several advantages can be seen for the latter application using water vapor as injectant rather than air. The increased density would lead to greater power production proportional to the increased mass flow. The more efficient transpiration cooling achieved due to the lower molecular weight and the higher specific heat would result in a larger energy storage at a given temperature level.

Another important aspect of the present work concerns the turbulent mixing analysis of the oxy-acetylene facility. Combustion gas torches and arc-plasma units have been widely used as experimental screening facilities for ablative systems due to their relatively low cost, availability, ease of operation, and reproducible results (22). Of these, the oxy-acetylene torch is perhaps the most widely used. Evaluation of the performance of the thermal protection in such facilities does not depend solely on properties of the tested material, but also on thermal, chemical, and physical interactions of the material with the environment. Examples of experimental evaluation of such facilities include work reported by Cutting, Fay, Hogan, and Moffatt (23). Tests were performed with known acetylene-oxygen mixtures in a shock tube. While environmental chemistry was considered in the energy transfer reported in the above work, thermal testing in an oxy-acetylene torch poses the added problem of mixing with the surrounding atmosphere.

CHAPTER III

THEORETICAL ANALYSIS

An evaluation of the thermal protection which can be achieved by a porous ceramic requires that the transient thermal response of the material be determined subject to the desired heat flux boundary conditions. The analysis presented in this chapter is formulated to predict transient temperature distributions in a porous, impregnated ceramic including coupling phenomena for a given environment. Effects of hydrate breakdown of the impregnate in the porous matrix, environmental chemistry, mass addition, and chemical reactions in the gas boundary layer are included.

Model for Porous Ceramic

The system studied consisted of a slip cast silica foam slab which contained a water-bearing gel as an impregnate. The foam used* was a porous matrix with a porosity of 0.60 and a density of 50 lbm/ft^3. The void space consisted of irregularly shaped pores, randomly spaced but sufficiently connected that vapor flow could be obtained through the porous matrix. A uniformly impregnated slab was assumed at a uniform initial temperature. Transient heating of the surface began with a sudden change in the free stream environment of the slab. The surface heat flux to the slab was dependent on these environmental

* Samples were supplied by GlasRock Inc., Atlanta, Georgia.

conditions, and also on the instantaneous conditions at the heated surface, e.g., $T(x = 0)$ and $\dot{m}_v$ $(x = 0)$. The temperature at which the hydrate breakdown occurs, T_v, is determined by a vapor-pressure relation for the gel in a manner similar to the vaporization of saturated liquids. Vaporization of the released water molecule takes place at increasing depths within the matix when the heat of vaporization is supplied. T_v was assumed to remain constant as the interface receded. Phenomena relating to the hydrate breakdown and interface model are discussed in detail in a subsequent section. Thus two distinct regions were assumed to exist in the porous matrix as indicated schematically by Figure 1, page 13.

Region I is next to the heated surface and consists of the porous, solid matrix with the vapor flow resulting from the impregnate dehydration. Vapor flow rates were low and the gas was assumed to be at the same temperature as the surrounding solid. All heat transfer and fluid flow was assumed to be one dimensional in the direction normal to the surface. Region II contains the unvaporized impregnate within the porous solid with the rear face assumed to be insulated and sealed to vapor flow such that vapor leaves only through the heated surface and counter to the direction of heat transfer.

Separating the two regions is an interface defined by the instantaneous location, x_v, of a temperature plane corresponding to the state at which impregnate breakdown occurs. A discontinuity in the slope of the temperature profile occurs at this interface due to the different thermal properties on either side and a net heat flux to the interface. The difference in heat flux on either side is

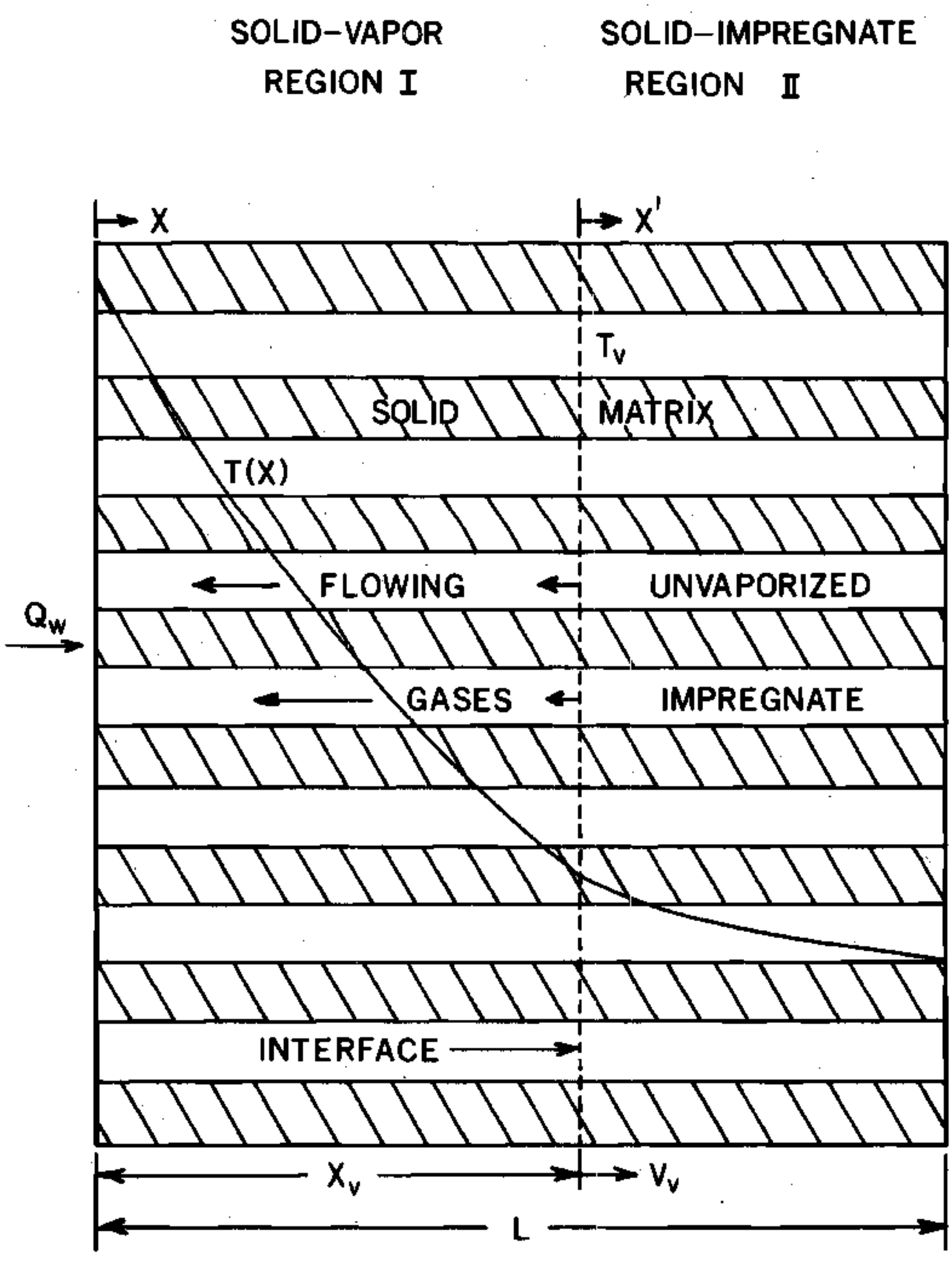

Figure 1. Schematic Drawing of Porous, Impregnated Ceramic

related by an energy balance to the rate of impregnate vaporization. This vaporization rate can then be used to determine the velocity at which the interface moves through the slab.

Energy Equations

Governing equations for the energy transfer in the two regions were obtained from an energy balance for the model described above. This is presented in Appendix A, page 104. The results are given below.

Region I

$$\rho_1 C_1 \frac{\partial T}{\partial \tau} = \frac{\partial}{\partial x}\left(k_1 \frac{\partial T}{\partial x}\right) + \frac{\partial}{\partial x}(\dot{m}\, h_T) \tag{3.1}$$

Region II

$$\rho_2 C_2 \frac{\partial T}{\partial \tau} = \frac{\partial}{\partial x}\left(k_2 \frac{\partial T}{\partial x}\right) \tag{3.2}$$

It is seen that the two equations differ only in the appropriate property values for the respective regions and in the convective enthalpy flux term appearing in equation 3.1. This term accounts for the energy flux associated with the vapor flow in Region I. The possibility of variable properties has been retained, however the condition of one dimensionality has been imposed.

Effective thermal properties defined by equation 3.3 were used for each region. Wiener (24) proposed these results as one of two bounding formulas for porous media.

$$k_1 = \sigma\, k_p + (1 - \sigma)\, k_d \tag{3.3}$$

$$\rho_1 C_1 = \sigma\, \rho_p C_p + (1 - \sigma)\, \rho_d C_d$$

The assumption of parallel thermal resistances of the solid and void regions results in an upper bound for the thermal conductivity given by equation 3.3. Minimum values are obtained by assuming thermal resistances in series. Deissler and Boegli (25) reported the variation between these limits as a function of the ratio of solid to void space conductivity. Using a value of k_d/k_p of seven, which corresponds to silica and water vapor, the difference in the upper and lower limits of effective conductivity is approximately 28 percent of k_d. Cheng (26) also reports that as k_d becomes greater than k_p, the effective conductivity tends to approach values predicted by equation 3.3. On this basis, equations 3.3 were used for effective properties of the porous media used in this investigation.

Boundary Conditions

Due to the mathematical nature of the two equations, two boundary conditions on position and one on time must be specified for the energy equation in each region. These are given below.

Region I

$$- k \left.\frac{\partial T}{\partial x}\right)_{x=0} = q_s(\tau) \; ; \; x = 0, \text{ all } \tau \tag{3.4}$$

$$T = T_v \; ; \; x = x_v, \text{ all } \tau$$

$$T = T_o \; ; \; \text{all } x, \; \tau = 0$$

Region II

$$T = T_v \; ; \; x = x_v, \text{ all } \tau \tag{3.5}$$

$$\frac{\partial T}{\partial x} = 0 \; ; \; x = L, \text{ all } \tau$$

$$T = T_o \ ; \ \text{all } x, \ \tau = \tau_o$$

Each of the above boundary conditions are easily implemented in the solution procedure with the exception of the heat flux, q_s, because of its complex dependency upon the solution for the porous slab and upon conditions at the gas-slab interface. For this reason, this boundary condition is treated separately in a later section. The solution technique for equations 3.1 and 3.2 is presented assuming at any given time that the surface heat flux, q_s, is known.

Moving Reference Frame

Due to the importance of the interface on the internal temperature profiles and on the surface heat flux through the vaporization rate, it is advantageous to formulate a moving coordinate system measured relative to the instantaneous interface position. Consider now the x', τ' coordinate system where x' is the instantaneous distance to a point in the slab relative to the interface as shown in Figure 1. The new coordinates are defined by:

$$x' = x - \int_o^\tau V_v \, d\tau \tag{3.6}$$

$$\tau' = \tau \tag{3.7}$$

Performing the coordinate transformation, equations 3.1 and 3.2 (Appendix A) respectively become:

Region I

$$\rho_1 C_1 \frac{\partial T}{\partial \tau'} = \frac{\partial}{\partial x'} \left\{ k_1 \frac{\partial T}{\partial x'} \right\} + \tag{3.8}$$

$$\dot{m} \frac{\partial h_T}{\partial x'} + \rho_1 C_1 V_v \frac{\partial T}{\partial x'}$$

Region II

$$\rho_2 C_2 \frac{\partial T}{\partial \tau'} = \frac{\partial}{\partial x'} \left\{ k_2 \frac{\partial T}{\partial x'} \right\} + \tag{3.9}$$

$$\rho_2 C_2 V_v \frac{\partial T}{\partial x'}$$

Since each of the boundary conditions are either in the form of constants or derivatives with respect to x, their form remains the same in the new coordinate system. It should be noted that the only change in the governing equations is the addition of the convective energy term which accounts for the slab movement into the differential control volume relative to an observer at the interface.

Interface

Before the solution to equations 3.8 and 3.9 can be obtained, equations for the interface velocity and mass flow rate of vaporized impregnate must be obtained. Figure 2 is a schematic drawing of the model at the interface.

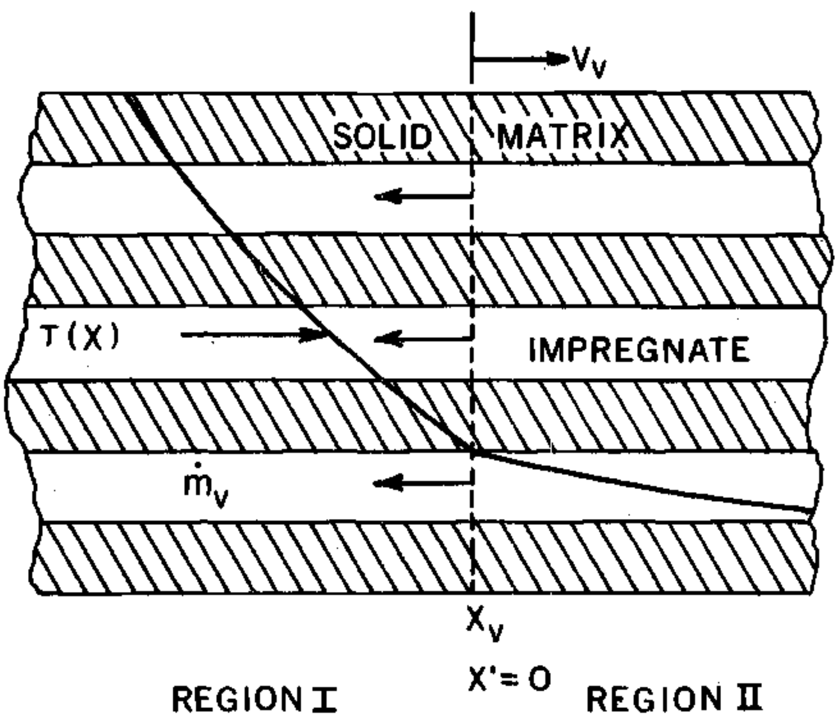

Figure 2. Schematic Drawing of Interface

The significant phenomena occuring here will be the hydrate breakdown and the resulting release and vaporization of the bound moisture. The hydrate chosen for study is that formed between gelatine and water. Gelatine is essentially protein for which six amino acids form approximately 90 percent of its composition (27). The phenomena of hydration is due to the polar properties of water which cause a binding of water dipoles to ions or ionic groups or to dipoles or polar groups. In the case of gelatine, it is the latter bond which effects hydration. According to the fibrillar theory, however, only a small portion of the water is actually involved in the hydration with the major portion held in the gel by capillary forces between the long, thread-like, protein chains in the gelatine (28). Haurowitz (29) states that gelatine gels are able to immobilize about 30 grams of water per gram of dry gelatine whereas the amount of water bound by hydration amounts to only .2 - .5 grams per gram of protein. The remainder of this water is "free". He further states that the hydrate bond energy for water and gelatine is approximately 3000 cal/gm mole of bound water. Based on these values, the energy required for hydrate breakdown is less than 0.05 percent of the energy required for water vaporization.

Thus the model chosen for the phenomena occuring at the interface will assume that an apparent heat of vaporization, Δh_v, is absorbed at the interface in vaporizing the water of hydration and free water molecules. It will be assumed that the only significance of the gelatine in the hydrate breakdown is in the difference of the vaporization temperature from that of pure water and in the contribution of the hydrate bond energy to Δh_v. Based on these assumptions, an energy balance at the interface yields,

$$\sigma \rho V_v \Delta h_v = - k_1 \frac{\partial T}{\partial x}\Big)_{x_v^-} + k_2 \frac{\partial T}{\partial x}\Big)_{x_v^+} \tag{3.10}$$

The quantity $\sigma\rho V_v$ represents the instantaneous mass rate of vaporization per unit total area at the interface and Δh_v represents the total energy per lbm required for dehydration and vaporization of the impregnate. Assuming that Δh_v is a constant, equation 3.10 yields the instantaneous mass flux into Region I and the instantaneous interface velocity. The assumption that Δh_v is constant is valid for constant pressure and temperature at the interface.

Method of Solution

A procedure for the simultaneous solution of equations 3.8, 3.9 and 3.10 was formulated subject to the prescribed boundary conditions. There are two significant factors in the formulation of equations 3.8 and 3.9 somewhat different from that of systems with surface phase changes. The first is that the phase transformation occurs at a transient location interior to the heated surface. The interface recession thus exhibits a somewhat greater dependence upon the transient response of the solid structure.

The second factor concerns the term in equation 3.8 accounting for the energy transfer associated with the gases released by interface vaporization. A corresponding phenomena does not exist in the governing equations for surface ablative systems. Thus it will be significant to determine the relative contribution of this term in comparison with other factors such as the impregnate phase change and heat capacity of the solid matrix. Criteria can then be established as to the relative importance of the latent heat of vaporization and vapor specific heat.

Solution for the Initial Period

In general the initial temperature of the slab will be less than that required for impregnate breakdown. An initial solution must be obtained for the period before surface vaporization begins for the transient temperature distribution of a finite slab under prescribed heat flux boundary conditions. If the environmental conditions are essentially constant and the surface temperature change up to the time vaporization begins is small, the surface heat flux can be assumed to be constant. For these conditions, the temperature distribution during this time is given by Carslaw and Jaeger (30) as:

$$T(x,\tau) = T_o + \frac{q_o L}{k_2}\left\{ \frac{\alpha_2 \tau}{L^2} + \frac{3x^2 - 6xL + 2L^2}{6L^2} - \right. \tag{3.11}$$

$$\left. \frac{2}{\pi} \sum_{n=1,2} \frac{1}{n^2} e^{-(n^2\pi^2\alpha_2\tau)/L^2} \cos(n\pi\, x/L) \right.$$

Setting $T(x, \tau) = T_v$, the time, τ_o, at which vaporization begins was obtained by trial and error. Iteration continued on τ_o until the surface temperature calculated from equation 3.11 was within 0.5 percent of T_v. The temperature distribution calculated at time τ_o was used as the initial distribution at the time surface vaporization begins.

Solution for the Vaporization Period

Equations 3.8 and 3.9 were non-dimensionalized by defining the following variables;

$$\overline{T} = \frac{T-T_v}{q_o L/k_r} \ , \ \overline{x} = x'/L \ , \ \overline{\tau} = \frac{\alpha_r \tau'}{L^2} \tag{3.12}$$

Where the reference properties k_r and α_r are defined by the effective values in Region I at the interface temperature. With these substitutions, the energy equations become

Region I

$$\frac{\partial \overline{T}}{\partial \overline{\tau}} = \left\{ \frac{\dot{m} C_v \alpha_1(T)}{\alpha_r k_1(T)} + \frac{LV_v}{\alpha_r} \right\} \frac{\partial \overline{T}}{\partial \overline{x}} + \tag{3.13}$$

$$\frac{\alpha_1(T)}{\alpha_r \ k_1(T)} \frac{\partial}{\partial \overline{x}} \left\{ k_1(T) \ \frac{\partial \overline{T}}{\partial \overline{x}} \right\}$$

Region II

$$\frac{\partial \bar{T}}{\partial \bar{\tau}} = \frac{\alpha_2}{\alpha_r} \frac{\partial^2 \bar{T}}{\partial \bar{x}^2} + \frac{LV_v}{\alpha_r} \frac{\partial \bar{T}}{\partial \bar{x}} \tag{3.14}$$

Due to coupling and non-linearity existing between the surface boundary condition and the governing equations, the solution was formulated for numerical integration on a high speed, digital computer. An explicit, forward difference formulation was used in the solution technique for the energy equations. The equations were linearized by evaluating all coefficients at temperatures known at a given time period.

Region I

$$\frac{\bar{T}(\bar{x}, \tau + \Delta\bar{\tau}) - \bar{T}(\bar{x}, \bar{\tau})}{\Delta\bar{\tau}} = \left\{ \frac{\dot{m}C_v\alpha_1}{\alpha_r\, k_1} + \right. \tag{3.15}$$

$$\left. \frac{LV_v}{\alpha_r} \right\} \left\{ \frac{\bar{T}(\bar{x} + \Delta\bar{x}) - \bar{T}(\bar{x}, \bar{\tau})}{\Delta\bar{x}} \right\} + \frac{\alpha_1}{\alpha_r k_1(\bar{x})} \frac{1}{\Delta\bar{x}}$$

$$\Bigg(k_1(x + \Delta x) \left\{ \frac{\bar{T}(\bar{x} + \Delta x, \bar{\tau}) - \bar{T}(\bar{x}, \bar{\tau})}{\Delta\bar{x}} \right. -$$

(equation cont.)

$$k_1(\bar{x}) \left\{ \frac{\bar{T}(\bar{x},\bar{\tau}) - \bar{T}(\bar{x} - \Delta\bar{x},\bar{\tau})}{\Delta\bar{x}} \right\} \Bigg)$$

Region II

$$\frac{\bar{T}(\bar{x},\bar{\tau} + \Delta\bar{\tau}) - \bar{T}(\bar{x},\bar{\tau})}{\Delta\bar{\tau}} = \frac{V_v L}{\alpha_r} \left\{ \frac{\bar{T}(\bar{x} + \Delta\bar{x},\bar{\tau}) - \bar{T}(\bar{x},\bar{\tau})}{\Delta\bar{x}} \right\} \tag{3.16}$$

$$+ \frac{\alpha_2}{\alpha_r} \left\{ \frac{\bar{T}(\bar{x} + \Delta\bar{x},\bar{\tau}) - 2\bar{T}(\bar{x},\bar{\tau}) + \bar{T}(\bar{x} - \Delta\bar{x},\bar{\tau})}{\Delta\bar{x}^2} \right\}$$

Before equations 3.15 and 3.16 can be integrated numerically, property data, interface velocity, and boundary conditions must be specified. Assuming that at any given time, τ', a temperature distribution, $\bar{T}(\bar{x},\bar{\tau})$, is known, property values are obtained from equations and values tabulated in Appendix C. The interface velocity, V_v, is obtained from equation 3.10 and the current temperature distribution. Forward and backward difference expansions about x_v as given by Wiley (31) were used respectively for the derivatives $\left.\frac{\partial\bar{T}}{\partial\bar{x}}\right)_{x_v^+}$ and $\left.\frac{\partial\bar{T}}{\partial\bar{x}}\right)_{x_v^-}$.

The boundary condition between Region I and II is fixed by the specification of interface temperature yielding $\overline{T}(x_v,\tau) = 0$. The insulated rear surface results in a zero temperature gradient for the last element of Region II.

Surface Boundary Condition

Up to this point, it has been assumed that the surface heat transfer is known in the formulation of the solution technique. At any instant of time however, the wall flux will be dependent upon the environmental conditions, surface temperature, surface chemistry, and mass addition into the boundary layer. The significance of the environmental conditions is not only in the free stream temperature and enthalpy, but also in the particular chemical species present in the free stream and their quantity. This will influence the species and their magnitude at the surface as will be discussed subsequently. Thus the surface heat flux is strongly coupled to the environmental conditions as well as to the transient temperature response for the vaporizing, porous slab.

A schematic drawing of the porous surface model depicting the phenomena to be considered is shown in Figure 3. It has been assumed that the surface mass transfer into the boundary layer occurs uniformly over the surface and that diffusion into the porous matrix by gaseous species in the boundary layer is negligible. Enthalpies shown are for the gaseous species crossing the surface and include the chemical enthalpy of formation for each component.

An energy balance for the model shown in Figure 3 yields

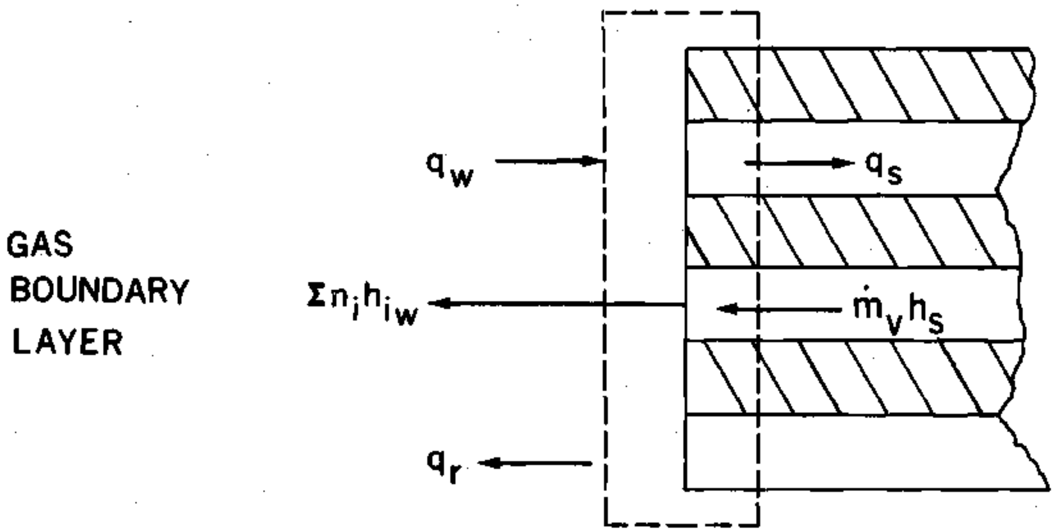

Figure 3. Schematic Drawing of the Heated Surface

$$q_s + q_R = q_w + \rho D_{12} \sum h_{iw} \frac{\partial Y_i}{\partial y} \Big)_w \tag{3.17}$$

$$- \rho v)_w \left\{ h_w - h_s \right\}$$

The first term on the right of 3.17 accounts for the conduction to the slab from the gas boundary layer and is dependent upon the surface mass transfer rate, the free stream temperature and chemistry. The next term accounts for the net energy flux due to diffusion at the surface and the last term includes chemistry and phase changes at the surface. The term q_R accounts for the net radiation heat transfer per unit area from the heated surface. Walton (32) reports that the net radiation from slip cast fused silica can be estimated from

$$q_R = .1714 . 10^{-8} \epsilon_R T_s^{4} \tag{3.18}$$

where ϵ_R is the apparent emissivity of the radiating surface. Walton reports ϵ_R to have a value between 0.6 and 0.7 below the softening temperature and between 0.3 and 0.4 above. Due to the rapid initial rise of surface temperature for the cases considered in this study, the emissivity will be assumed constant and equal to 0.3 for all calculations involving thermal radiation. Equation 3.17 can be rewritten in terms of the stagnation enthalpy to obtain

$$q_s + q_R = \frac{k}{c} \frac{\partial I}{\partial y} \Big)_w + (Le - 1) \sum h_i \frac{\partial Y_i}{\partial y} \Big)_w - \rho v)_w (h_s - h_w) \tag{3.19}$$

The stagnation enthalpy is introduced to facilitate the use of results of boundary conditions obtained from the jet mixing analysis discussed in a subsequent section. At any given time, the surface temperature, T_w, and mass addition, $\rho v)_w$ were known from the solutions of the energy equations for Regions I and II for the previous time period. However the surface mass fractions and the gradients of enthalpy and Y_i remain to be determined in the above equation. This must come from an analysis of the conservation equations for a chemically reacting boundary layer with surface mass addition.

Gas Boundary Layer

The conservation equations for the steady, axisymmetric, chemically reacting, boundary layer flow of a multicomponent gas over a blunt body from Dorrance (33) are:

Continuity

$$\frac{\partial}{\partial s}(\rho u r) + \frac{\partial}{\partial y}(\rho v r) = 0 \tag{3.20}$$

Momentum

$$\rho u \frac{\partial u}{\partial s} + \rho v \frac{\partial u}{\partial y} = \frac{\partial}{\partial y}\left\{ \mu \frac{\partial u}{\partial y} \right\} + \rho_e U_e \frac{\partial u_e}{\partial s} \tag{3.21}$$

Energy

$$\rho u \frac{\partial I}{\partial s} + \rho v \frac{\partial I}{\partial y} = \frac{\partial}{\partial y}\left\{ \frac{\mu}{Pr} \frac{\partial I}{\partial y} \right\} + \mu(1 - \frac{1}{Pr}) \tag{3.22}$$

(equation cont.)

$$\frac{1}{2}\frac{\partial U^2}{\partial y} - \frac{\partial}{\partial y}\left\{\left(\frac{1}{Le} - 1\right)\rho D_{12}\sum h_i \frac{\partial Y_i}{\partial y}\right\}$$

Species

$$\rho u \frac{\partial Y_i}{\partial s} + \rho v \frac{\partial Y_i}{\partial y} = \frac{\partial}{\partial y}\left\{\rho D_{12}\frac{\partial Y_i}{\partial y}\right\} + \dot{w}_i \qquad (3.23)$$

It is assumed the gas boundary layer can be approximated as an effective binary mixture with one diffusion coefficient, D_{12}, applicable for diffusion of all species. Solutions to the equations given above yield the wall gradients necessary to evaluate the surface heat transfer. This solution should account for the effects of surface mass addition, Pr not equal to one, chemical reactions, and blunt-body geometry, $\left(\frac{\partial p}{\partial s} \neq 0\right)$. When considering chemical reactions, a source term accounting for the generation of a given species complicates the species equation. This difficulty can be overcome by writing the conservation of species equation in terms of the element mass fraction $\overline{Y}_k$ as suggested by Lees (12). Equation (3.23) then becomes

$$\rho u \frac{\partial \overline{Y}_k}{\partial s} + \rho v \frac{\partial \overline{Y}_k}{\partial y} = \frac{\partial}{\partial y}\left\{\rho D_{12}\frac{\partial \overline{Y}_k}{\partial y}\right\} \qquad (3.24)$$

where

$$\overline{Y}_k = \sum r_{i,k} Y_i$$

and $r_{i,k}$ represents the ratio by mass of element k in species "i".

Solutions to Boundary Layer Equations

Equations 3.21, 3.22 and 3.24 are transformed into ordinary differential equations by introducing independent variable transformations defined as follows:

$$\eta = \frac{\rho_e u_e r}{(2\overline{s})^{\frac{1}{2}}} \int_o^y \frac{\rho}{\rho_e} \, dy \qquad (3.25)$$

and

$$\overline{s} = \int_o^s \rho_e \mu_e r^2 u_e ds \qquad (3.26)$$

and the following non-dimensional dependent variables:

$$f'(\eta) = u/u_e(s) \tag{3.27}$$

$$Z_k(\eta) = \overline{Y}_k/\overline{Y}_{ke}(s)$$

$$g(\eta) = I/I_e(s)$$

The transformed equations, (see e.g. Dorrance) are

$$(cf'')' + ff'' + \frac{2\overline{s}}{ue}\frac{due}{d\overline{s}}\left\{ \frac{\rho e}{\rho} - f'^2 \right\} = 0 \tag{3.28a}$$

$$\left(\frac{c}{Pr} \; g' \right) + fg' = \frac{2\overline{s}f'}{Ie} \; g \; \frac{dIe}{d\overline{s}} + \left\{ \frac{c}{Sc} \left(\frac{1}{Ie} - 1 \right) \right. \tag{3.28b}$$

$$\left. \sum \frac{h_i Y_{ie}}{Ie} Z_i \right\}' + \frac{ue^2}{Ie}\left\{ \left(\frac{1}{Pr} - 1 \right) cf'f'' \right\}'$$

and

$$\left(\frac{c}{Sc} Z_i' \right)' + fZ_i' = \frac{2\bar{s}f'Z_i}{\bar{Y}_{ie}} \frac{d\bar{Y}_{ie}}{d\bar{s}} \tag{3.28c}$$

where

$$C = \frac{\rho\mu}{\rho_e\mu_e}$$

For the case of axisymmetric stagnation flow, Schlichting (34) suggests a potential flow solution of the form, $u_e = as$.

Assuming the product $\rho\mu$ is constant, it can then be shown that

$$\frac{2\bar{s}}{ue} \frac{due}{d\bar{s}} = \frac{1}{2}$$

Introducing non-dimensional variables $\pi_T(\eta)$ and $\pi_{AB}(\eta)$ defined by

$$\pi_T = \frac{g - g_w}{1 - g_w} , \tag{3.29}$$

and

$$\pi_{AB} = \frac{Z_i - Z_{iw}}{1 - Z_{iw}} ,$$

equations 3.27, 3.28 and 3.29 become, for an axisymmetric stagnation point:

$$f''' + ff'' + \beta(1 - f'^2) = 0 \tag{3.30}$$

where $\beta = \frac{1}{2}$

$$\pi_T'' + Pr\ f\ \pi_T' = 0 \tag{3.31}$$

and

$$\pi_{AB}'' + Sc\ f\ \pi_{AB}' = 0 \tag{3.32}$$

for Le = 1, $\rho\mu$ = constant, $\rho/\rho e$ = 1 and constant Prandtl and Schmidt numbers. The latter assumption is not necessary when the last term of equation 3.30 is not significant as has been suggested by Lees (12).

Elzy and Sisson (35) have obtained the numerical solution for a set of equations in the form of 3.30, 3.31, and 3.32 with equivalent boundary conditions. Tabulated results are given for dimensionless distributions and gradients of the dependent variables. From the definition of the dimensionless velocity function, it can be shown that

$$f(0) = \frac{-\ \rho v)_w}{\sqrt{2\rho e \mu e \frac{due}{ds}}} \tag{3.33}$$

By using solutions tabulated for f(0) calculated from a known value of $\rho v)_w$, surface injection is considered in the results for the wall gradients. Substitution of the nondimensional variables into equation 3.19 yields

$$q_s + q_R = \frac{1}{Pr}\sqrt{2\ \rho e \mu e\ \frac{due}{ds}}\ (Ie - Iw) \qquad (3.34)$$

$$\pi_T'(0) - \rho v)_w\ (hw - hs)$$

It would appear that the last term in equation 3.34 is a "blowing" effect on heat transfer. This term however accounts only for phase changes and/or chemical reaction of the injected fluid at the porous surface. The true blowing effect on heat transfer is accounted for in the quantity $\pi_T'(0)$ which could more exactly be written as $\pi_T'(0, \beta, f(0), Pr)$ indicating its dependence upon pressure gradient, mass injection, and fluid properties. Thus not only does vaporization and sometimes chemical reactions occur at a surface with mass injection, but also occuring is the effect of surface injection upon the boundary layer profiles. The above equation also indicates the possibility for surface heat transfer to be increased with mass injection. This has been suggested by Scala and Gilbert (18) and is possible if the last term of equation 3.34 is negative. Consider the case where a significant quantity of molecular hydrogen is injected at moderate temperatures in a boundary layer with excess oxygen. Under conditions of thermodynamic equilibrium the exothermic formation of any significant quantity of water vapor would cause the latter term to be negative and contribute to an increase in heat transfer.

The evaluation of equation 3.34 is highly coupled to the transient thermal response of the porous slab. As will be discussed subsequently, surface temperature and injection rate are required to determine the surface chemistry. Surface chemistry and temperature are needed to determine h_w, h_s, and I_w. The injection rate in addition to appearing in the last term must be known to evaluate the wall gradient, $\pi_T'(0)$. In addition to these factors the environmental chemistry will significantly influence the wall fluxes through the environmental enthalpy and surface concentrations.

Lees (12) suggests that results for surface heat transfer for a reacting gas can be obtained independently of the boundary layer rate chemistry model for the case of unity Lewis number. The necessity of realistic surface chemistry becomes significant however in the evaluation of the wall concentrations and subsequently the wall enthalpy. This has already been demonstrated by the variation of wall enthalpy at 2000°K in the work by Weston (17). It is felt this will be most significant when injecting a foreign species into a given environment, e.g. H_2O into air, as opposed to air into air as this would lead to a larger shift in the element distribution with injection rate. Effects of environmental chemistry are thus not restricted to the last term of equation 3.34. Free stream composition is also significant in the evaluation of any quantity which is dependent upon surface composition as will be seen in the following section.

Surface Chemistry Evaluation

The problem is now to determine the surface mass fractions of the individual species for a known environmental chemistry, surface temperature, and mass injection rate into the boundary layer. The first choice would be to obtain the solution to the conservation of species equation for the prescribed boundary conditions. However, as mentioned previously, when chemical reactions occur in the boundary layer, these solutions become very difficult to obtain due to the generation term occuring in the species equation. As discussed previously, this difficulty is overcome by writing the conservation of species equation in terms of an element mass fraction, $\overline{Y}_k$.

The sum of the bulk and diffusion flow for an effective binary mixture, can be written as follows:

$$n_{iy} = - \rho D_{12} \frac{\partial Y_i}{\partial y} + Y_i \sum n_{iy} \tag{3.35}$$

In a manner analogous to the procedure for the conservation of species equation, this can be written for element k to obtain

$$\overline{n}_{ky} = - \rho D_{12} \frac{\partial \overline{Y}_k}{\partial y} + \overline{Y}_k \sum \overline{n}_{ky} \tag{3.36}$$

where equation 3.36 is the total mass flux of element k. Substitution of the non-dimensional variables defined in equations 3.25 yields after evaluating at the wall

$$\bar{n}_{kw} = -\frac{1}{Sc}\sqrt{2\rho e\mu e\,\frac{due}{ds}}\left\{\bar{Y}_{ke} - \bar{Y}_{kw}\right\}\pi'_{AB}(0) \qquad (3.37)$$

$$+\bar{Y}_{kw}\,(\rho v)_w$$

Substituting equation 3.33 for $\rho v)_w$ and simplifying we obtain

$$\frac{\bar{Y}_{kw} - \phi_k}{\bar{Y}_{kw} - \bar{Y}_{ke}} = \frac{\pi'_{AB}(0)}{Scf(0)} \qquad (3.38)$$

where

$$\phi_k = \frac{\bar{n}_{kw}}{\rho v)_w} \qquad (3.39)$$

represents the mass fraction of element k in the fluid being injected. Defining a blowing parameter B by the relation

$$B = \frac{\pi'_{AB}(0)}{Scf(0)} \tag{3.40}$$

equation 3.39 becomes

$$\overline{Y}_{kw} = \frac{\phi_k - \overline{Y}_{ke} B}{1 - B} \tag{3.41}$$

Equation 3.41 yields the desired surface element concentrations for a known injection rate f(0), geometry and free stream conditions $\overline{Y}_{ke}$. However, before the surface species concentrations can be obtained, the surface chemistry model must be specified. For the assumption of chemical equilibrium, species concentrations can be obtained from the results of equation 3.41 and the following information:

Temperature at gas-solid interface,

Species being considered,

Element balance for all elements,

Equilibrium constants.

A system of N equations are obtained for the mass fractions of the N species being considered. These are given in Appendix B for the system in consideration along with the method used for their solution.

At this point it is noted that the freestream environmental conditions have been assumed known in the analysis. This information, including freestream temperature, enthalpy, and chemistry, must be determined for the particular environment to be studied. An analysis was carried out to obtain the above properties for the experimental testing environment used for this study, combustion of an oxygen and acetylene jet in a stagnant atmosphere of air.

Turbulent Jet Mixing Analysis

The analysis to determine the chemical and thermal characteristics of a reacting jet must account for the chemical interaction and mixing of the jet with the surrounding atmosphere. Figure 4 schematically represents the exhaust of the jet into the surrounding atmosphere. It is assumed the jet is a known, axisymmetric mixture of C_2H_2 and O_2 which exhausts and mixes with atmospheric O_2 and N_2. The governing equations for a similar H_2, O_2 system in supersonic combustion have been presented by Libby (36) and are given below.

$$\rho u \frac{\partial u}{\partial z} + \rho v \frac{\partial u}{\partial r} = \frac{1}{r} \frac{\partial}{\partial r} \left(\epsilon \rho r \frac{\partial u}{\partial r} \right) \tag{3.42}$$

$$\rho u \frac{\partial I}{\partial z} + \rho v \frac{\partial I}{\partial r} = \frac{1}{r} \frac{\partial}{\partial r} \left(\epsilon \rho r \frac{\partial I}{\partial r} \right) \tag{3.43}$$

$$\rho u \frac{\partial Y_i}{\partial z} + \rho v \frac{\partial Y_i}{\partial r} = \frac{1}{r} \frac{\partial}{\partial r} \left(\epsilon \rho r \frac{\partial Y_i}{\partial r} \right) + \dot{w}_i \tag{3.44}$$

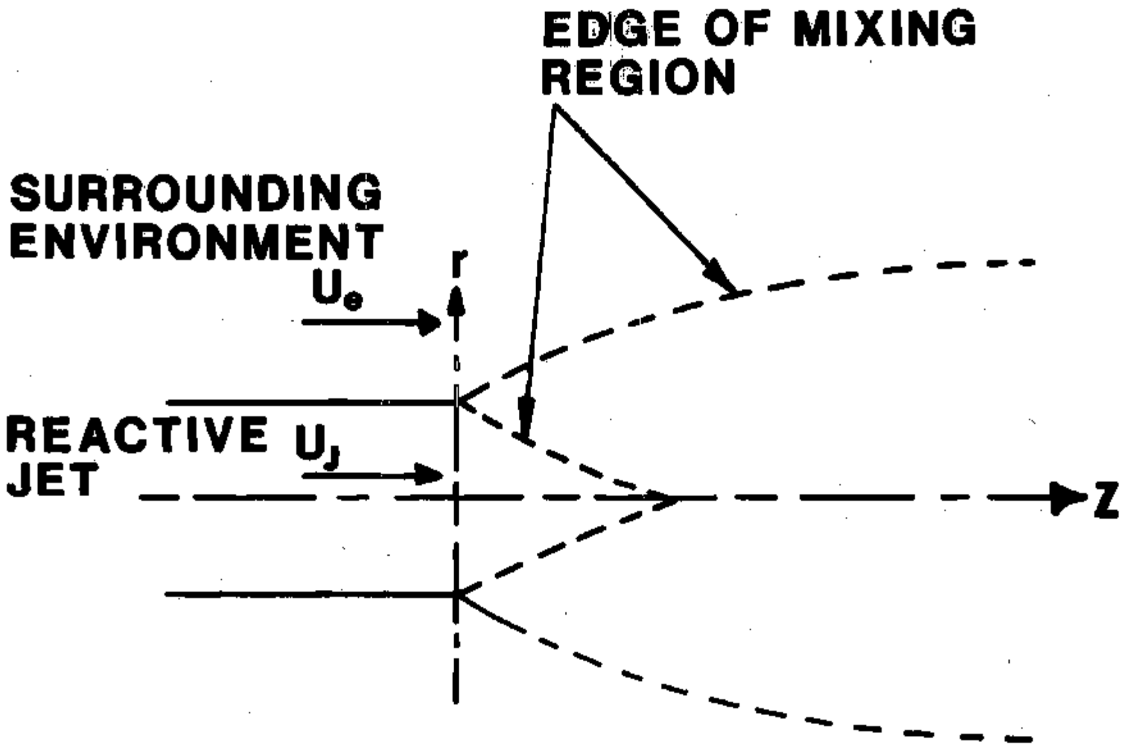

Figure 4. Jet Mixing Region

Gaseous radiation and free convection have not been considered and the turbulent Lewis and Prandtl numbers are assumed to be unity. The above equations each possess similar terms with the exception of the chemical generation term of 3.44. This term can only be neglected for frozen flow which would generally not be applicable for low speed, multicomponent flows of a fuel and an oxidizer (36). This difficulty is again overcome with the previously mentioned suggestion by Lees (12) by rewriting 3.44 for conservation of elemental mass. As elements are conserved when considering chemical reactions, the chemical generation term, $\dot{w}_i$, is identically zero, yielding the result

$$\rho u \frac{\partial \overline{Y}_k}{\partial z} + \rho v \frac{\partial \overline{Y}_k}{\partial r} = \frac{1}{r} \frac{\partial}{\partial r}\left(\epsilon \rho r \frac{\partial \overline{Y}_k}{\partial r}\right) \qquad (3.45)$$

where $\overline{Y}_k$ represents the local mass fraction of element "i". The similarity of equations, 3.42, 3.43 and 3.45 suggests the possibility of similar solutions such that

$$\frac{u - u_J}{u_e - u_J} = \frac{I - I_J}{I_e - I_J} = \frac{\overline{Y}_k - \overline{Y}_{kJ}}{\overline{Y}_{ke} - \overline{Y}_{kJ}} \qquad (3.46)$$

After defining the non-dimensional velocity, U, equations 3.47 follow from 3.46.

$$I = \frac{U_J(U_e - U) + Ie(U - 1)}{(Ue - 1)} \tag{3.47a}$$

$$\overline{Y}_k = \frac{\overline{Y}_{kJ}(Ue - U) + \overline{Y}_{ke}(U - 1)}{(Ue - 1)} \tag{3.47b}$$

where

$$U = u/u_J \tag{3.47c}$$

It is noted that the above results differ from those of Libby for a jet exhausting into an atmosphere with finite velocity. They are easily obtained however from the essence of his analysis and by following his suggestion for the case of a quiescent atmosphere.

Experimental justification for the above analysis is available in the literature. In a report on similar solutions for turbulent mixing, Donovan (37) reports that the flow becomes similar beyond an axial position of about 14 jet radii. An experimental study by Chriss (38) reports that profile similarity of composition, velocity, and total enthalpy is a valid assumption for subsonic mixing of hydrogen and air jets. He further found that unity turbulent Lewis number was a valid assumption for jet to outer region density ratios down to 0.08.

From the results of equations 3.47, solutions for the variation of free stream element mass fraction and stagnation enthalpy in the test environment were obtained as a function of the decay of the non-dimensional, centerline velocity. Experimental measurement of the stagnation pressure variation and the jet velocity as described in the following chapter allowed these results to be transformed into the physical plane for the oxy-acetylene experimental facility. Willbanks (39) has also previously used a similar application of the results of Libby to determine the distribution of species mass fraction and total enthalpy for frozen, supersonic flow in the exhaust of an oxy-hydrogen rocket motor. Final specification of species distribution and adiabatic flame temperature required a double trial and error procedure using the results of equation 3.47 and Appendix B.

For a given non-dimensional velocity, U, equations 3.47 yield the local stagnation enthalpy, I, and element mass fraction, $\overline{Y}_k$. A local flame temperature was then assumed. With these values, the analysis of Appendix B was imposed to yield trial values of species mass fractions for the assumed temperature. These were used to calculate a test value of the stagnation enthalpy which was compared to the value predicted by equation 3.47a. The difference in the two values was used to modify the assumed temperature and the procedure was repeated until the calculated and predicted values agreed within one percent.

This was repeated for successive values of U until the desired distribution was obtained. It is noted that once the above results were obtained for temperature and concentration distributions, thermal and transport properties for the species and the mixture were determined with the relations of Appendix C.

Property Data

Thermodynamic and transport property data used in this analysis are summarized in Appendix C. Chemical enthalpy, viscosity, specific heat and equilibrium constants were required for the equilibrium turbulent mixing analysis. Thermal analysis of the transient heating of the porous slab required the above data in addition to specific heat of water vapor and thermal conductivity for Regions I and II. The equations used and their sources are given for the species and property ranges of this investigation.

The solutions for non-dimensional wall gradients for equations 3.30, 3.31, and 3.32 are also given as a function of the injection parameter, f(0).

Iteration Procedure

At any given time, the internal temperature distribution in the porous slab was known from the previous numerical integration. Before the difference equations for each region were solved for the following time interval, the boundary conditions for the next time period were determined.

Equation 3.10 was applied to the known temperature profiles to determine the vaporization rate. The surface element mass fractions were then obtained from equations 3.41, 3.47b and data for $\pi'_{AB}(0)$.

Knowing the element concentrations and surface temperature, the surface species mass fractions and subsequent enthalpy were determined from the analysis of Appendix B. Equation 3.34 was evaluated to determine surface heat transfer for the above conditions. Equations 3.15 and 3.16 were then integrated numerically to obtain the temperature profile for the next time period and then the procedure was repeated.

CHAPTER IV

EXPERIMENTAL INVESTIGATION

The experimental portion of the investigation was divided into two parts. Tests were made to analyze experimentally the thermal environment produced by an oxy-acetylene combustion facility. This included measurement of stagnation heat transfer and pressure for a range of operating conditions. The second phase consisted of a series of heat transfer tests on porous, impregnated ceramic samples during which the transient temperature variations in the samples were monitored.

Oxy-acetylene Facility

A schematic drawing of the oxy-acetylene test facility is shown in Figure 5. A list of the apparatus used in the facility is given in Table 1.

The fuel and oxidizer line pressure were held constant by the two-stage pressure regulators listed in Table 1. Fuel and oxidizer flow rates were determined by the Metco flow meter. Calibration curves for each gas were supplied by the manufacturer. Control of the fuel and oxidizer flow rates was maintained by adjustment of individual needle values on the mixing chamber. Accuracy of the calibration curves was not specified by the manufacturer; however the flowmeter could be read to within one SCFH (standard cubic foot per hour) and estimated to approximately 0.5 SCFH.

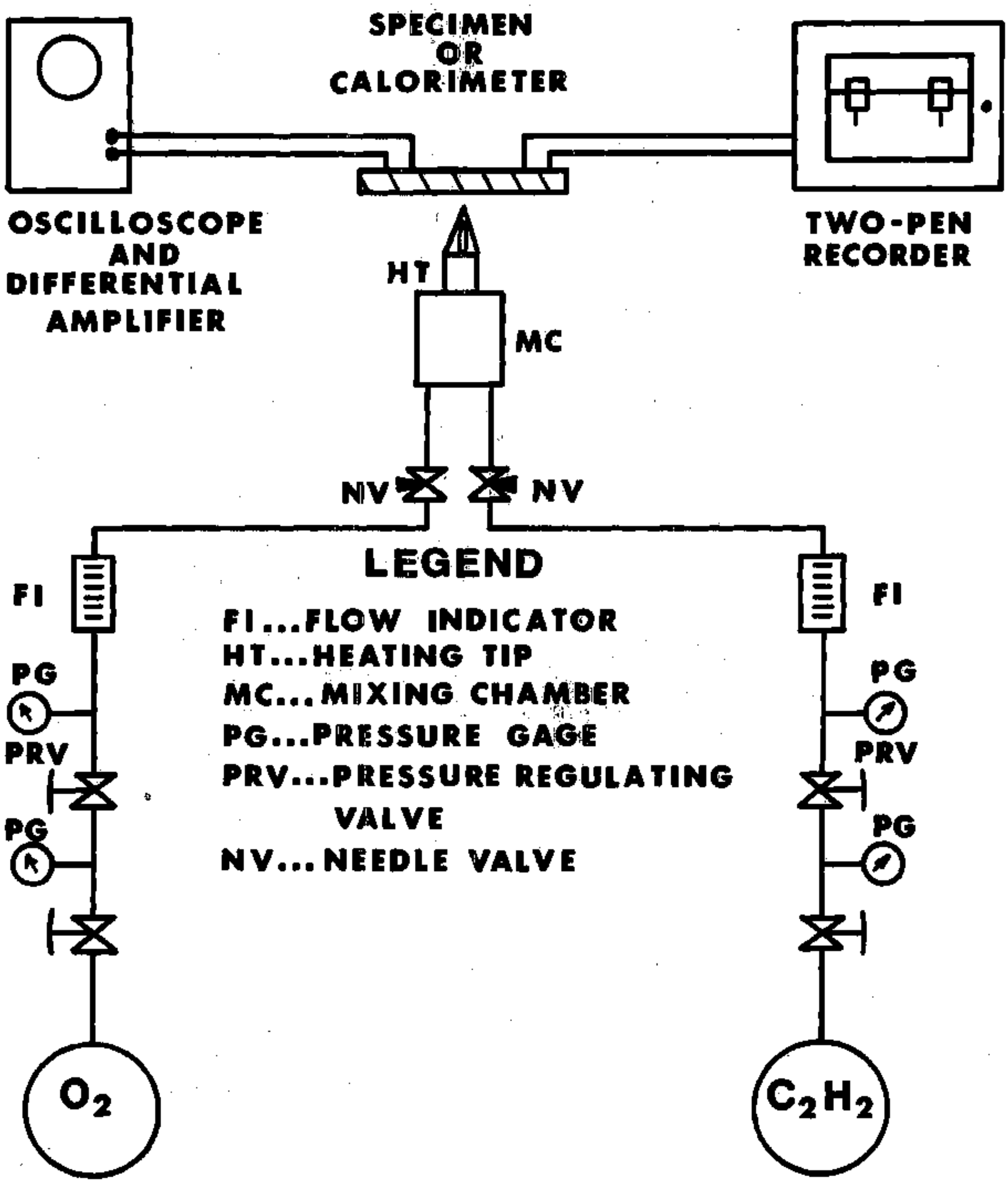

Figure 5. Oxy-acetylene Combustion Facility

Table 1. List of Oxy-acetylene Combustion Equipment

Oxygen regulator	AIRCO Model 806-8456
Acetylene regulator	AIRCO Model 806-8402
Heating Tip	AIRCO Model 9903-7
Mixing Chamber	AIRCO Model 9221
Flowmeter	Metco Type GF
Recorder	Honeywell Electronik 17
Oscilloscope	Tektronix Type 3B3
Differential Amplifier	Tektronix Type 2A63

Calorimeter

Heat flux measurements were made using a Hy-Cal Engineering, Model C-1300-A-150-072 water cooled calorimeter. The calorimeter had a calibrated linear d-c output signal of 0-5.5 mv for a surface heat flux of 0-150 BTU/ft^{2}sec. Diameter of the sensor area was 0.182 inches. Accuracy was ± 3 percent with a sensitivity of 10 millivolts per solar constant (0.123 BTU/ft^{2}sec). The output signal was monitored by the oscilloscope and differential amplifier unit listed in Table 1. A typical output from the calorimeter is shown in Figure 6. The vertical scale is one millivolt per division and the 4.9 millivolts shown indicates a heat flux of 136 BTU/ft^{2}sec from the calibration curve.

Temperature Recorder

The transient temperature variations in the samples tested were monitored by a Honeywell Electronik 17, Model 153028, two pen recorder. The recorder had a one second full scale balance speed and range change kits for full scale balance speed and range change kits for full scale

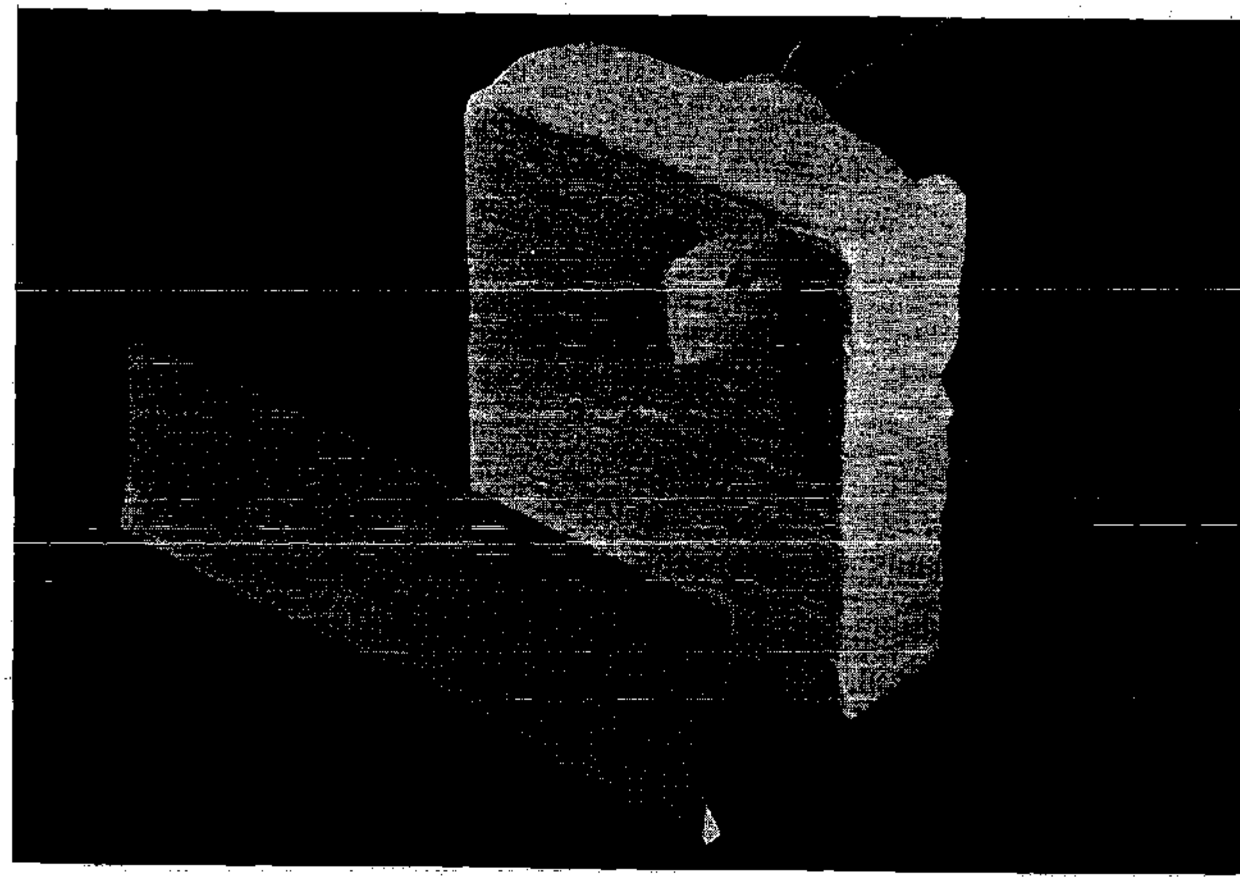

Figure 6. Typical Output from Heat Flux Calorimeter.

temperature measurements of 0-2500°F and 0-500°F using chromel-alumel thermocouples. The recorder accuracy and sensitivity were respectively ± 0.25 percent and 1°F for the 2500°F range and ± 1.5°F and 0.5°F for the 500°F range. The sensitivity will be important concerning subsequent comments on the measured interface position.

Stagnation Pressure Probe

Figure 7 gives a schematic of the apparatus used for centerline stagnation pressure measurements. By activating the linear positioner, the pressure probe could be moved in and out of the flame along the jet axis and thus obtain the centerline stagnation pressure distribution. The pressure was measured by a two inch, Ellison inclined draft gage. This gage was calibrated to read pressure differences up to two inches of water to the nearest one hundredth of an inch.

Experimental Procedure

Heat Flux Measurements

The stagnation point heat flux of the oxy-acetylene torch was measured for acetylene flow rates from 15 to 40 SCFH at distances of two to three inches form the torch tip. The calorimeter was attached to a support arm mounted on a horizontal bearing such that the calorimeter could be rotated into a fixed position on the centerline of the torch exhaust. To obtain a heat flux measurement, the calorimeter was first attached to the support mechanism at the desired distance from the torch tip. After removing the calorimeter from in front of the torch, the gases were ignited and the flow rates adjusted to the desired values as indicated by the flow meter. In all cases the

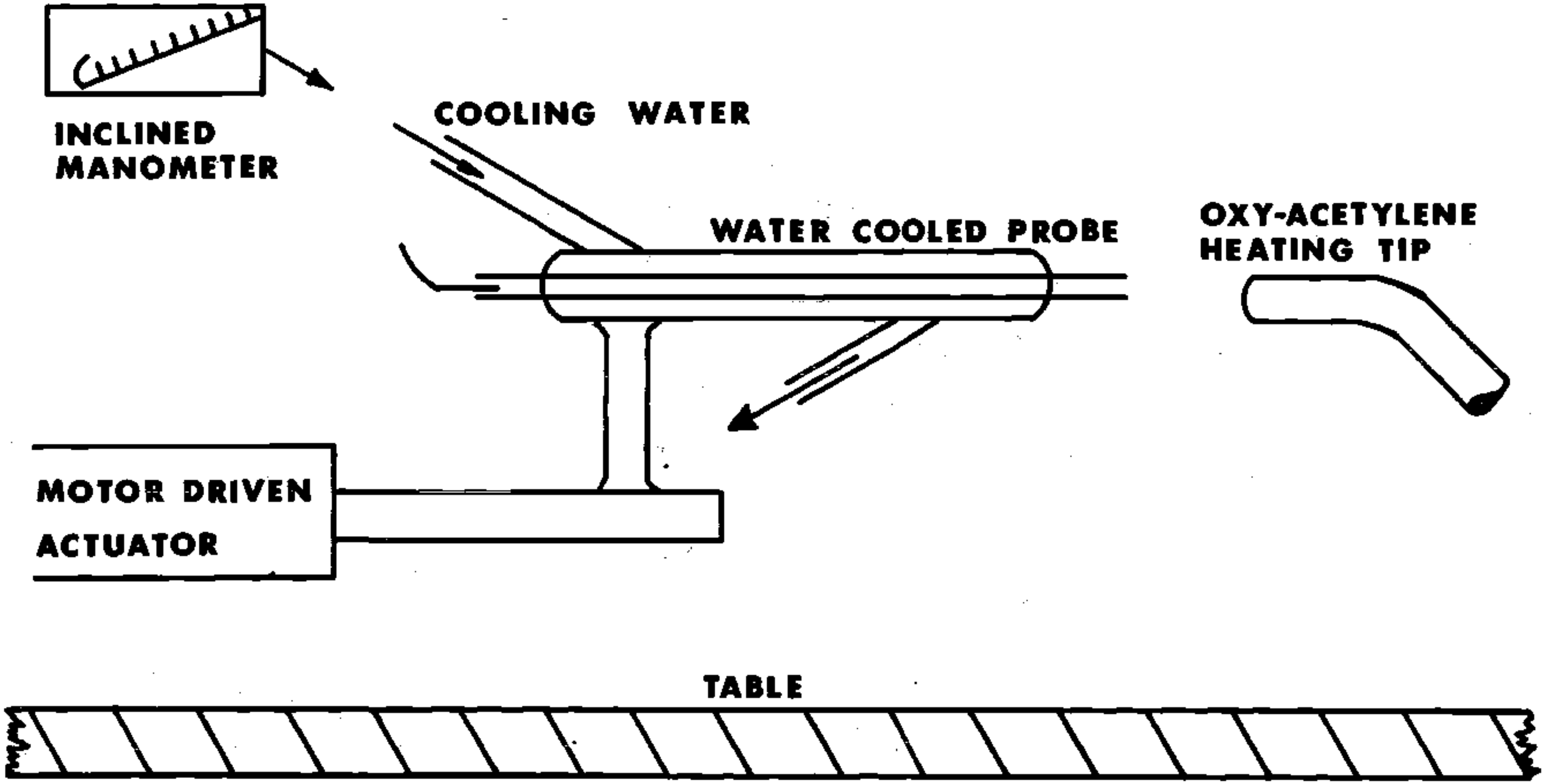

Figure 7. Stagnation Pressure Measurement Apparatus

air:fuel ratio was maintained at 1.2:1, ± 10 percent, as recommended by ASTM (40). Once the desired flow conditions were obtained, the calorimeter was rotated into a fixed position on the centerline and the sweep on the oscilloscope simultaneously triggered. After approximately three seconds, the calorimeter was rotated away from the flame and the resulting output shown on the oscilloscope was photographed.

It is seen from Figure 6 that the calorimeter output remained essentially constant during the test indicating a constant cold-wall heat flux and also that the output returned to the zero base line after the flame was removed. This procedure was repeated to obtain the desired data for subsequent gas flow rates and calorimeter positions.

Stagnation Pressure Measurements

The apparatus shown in Figure 7 was used to measure the centerline stagnation pressure distribution in the oxy-acetylene facility for a range of air-fuel flow rates. This information was used to determine the centerline velocity distribution required in the analysis of Chapter III.

Initially the probe was mounted on the actuator and aligned such that the actuator moved the probe along the axis of the torch facility. This alignment was made by measurement from fixed reference points and by adjustment to the point of maximum stagnation pressure at successive distances from the torch exit. The torch was then ignited and the gas flow rates adjusted to desired values. Centerline pressure measurements were then recorded as the probe was moved in and out of the flame.

This procedure was repeated for a range of gas flow rates. Measurements were made from six inches to within one and one-half inches of the torch tip.

Impregnated Ceramic

The final portion of the experimental investigation was concerned with the thermal evaluation of the porous, impregnated, ceramic samples. Ceramic samples were cut four inches square from plates of 50 lbm/ft^3 silica foam which were approximately 0.9 inches thick. Figure 8 shows a typical cemented sample with thermocouple leads and dowel support.

At least two thermocouples were placed in each sample tested. They were constructed from Leeds & Northrup, 28 gage chromel-alumel thermocouple wire covered with asbestos insulation. Thermocouples were placed at the desired depths ranging from 3/16 to 0.9 inches from the heated surface with the junction located in the center of the slab as shown in Figure 9. The leads were then brought out the sample sides parallel to the heated surface to minimize thermal gradients along the thermocouple wire. Pilot holes for the thermocouples were approximately 0.054 inches in diameter and were drilled with a number 54 drill.

The four sides of the sample and the back surface were covered with silica cement to provide thermal insulation and a vapor seal for the impregnate. This insured that the vaporized impregnate passed through the heated surface. Dowel pins 0.375 inches in diameter were cemented in the center of the rear face to provide a support for the sample.

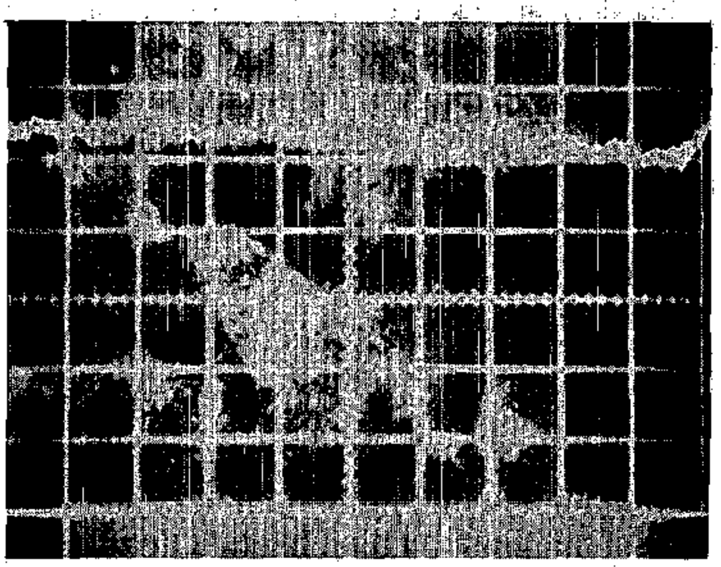

Figure 8. Photograph of a Typical Sample

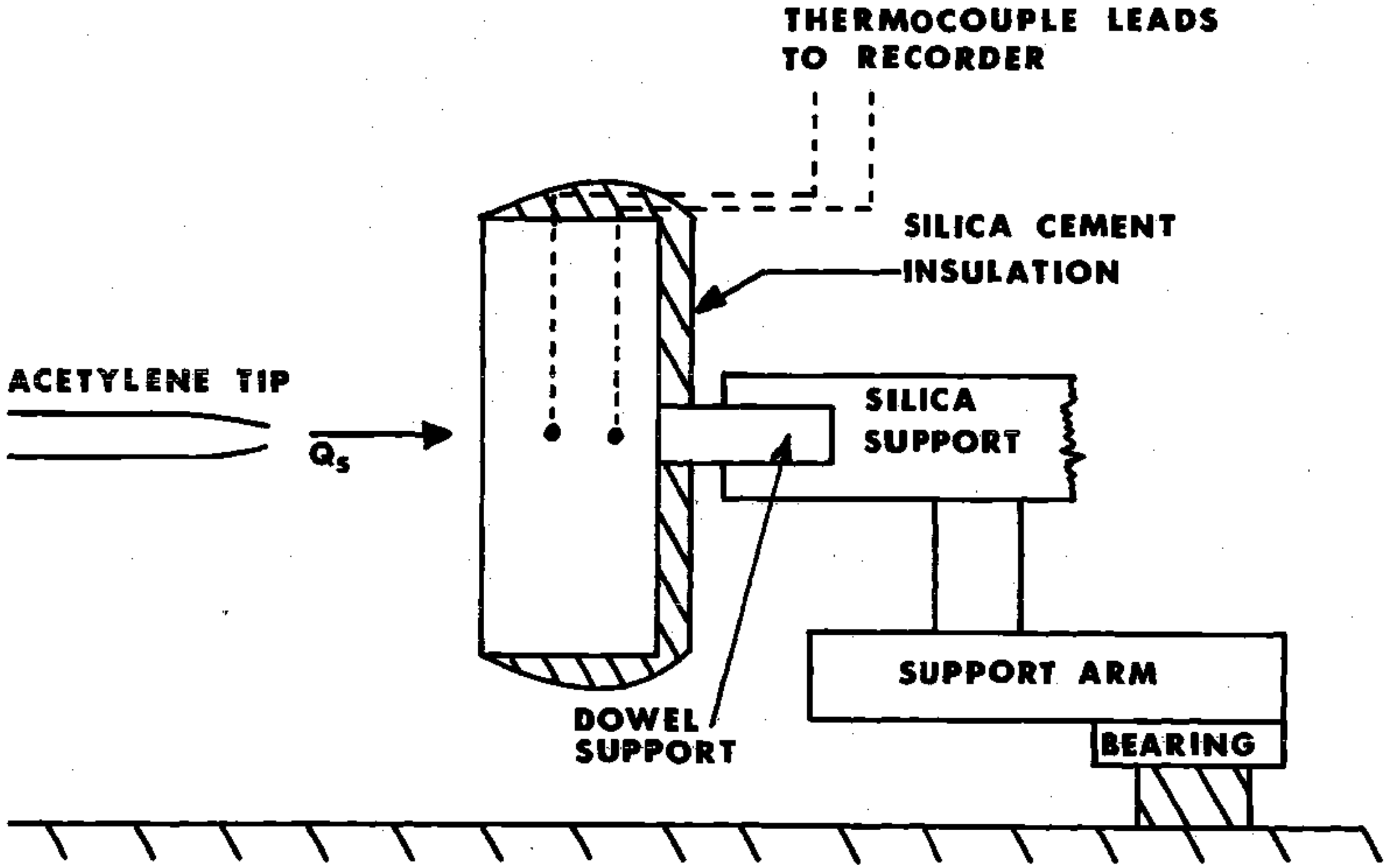

Figure 9. Silica Foam Test Sample

A liquid, gelatine impregnate was then put in the porous sample. The impregnate used was Knox, unflavored gelatine. In order to impregnate the porous sample the test pieces were placed in a vacuum chamber which was then evacuated. Liquid gelatine was then bled into the chamber, air pressure reimposed and the sample refrigerated in order to gel the impregnate.

To prepare for a test, a holder fitted to the dowel support on the sample was fastened on the rotating arm described previously. This arm was in the shape of a "Y" such that both the heat flux transducer and a ceramic sample could be successively rotated into the torch exhaust. Placement of the holder on the arm was such that the sample was centered in the torch exhaust at the desired distance from the tip when the dowel was inserted into the holder and the arm rotated to a predetermined position.

Figure 9 is a schematic drawing of a sample in position in the torch exhaust. A second arm attached to the rotating bearing provided a support for the calorimeter. This allowed the initial cold-wall heat flux to be measured at the desired test conditions immediately before the sample test began. This was done on approximately half of the tests as a check on the previously determined heat flux.

The procedure for a typical test run was first to mount and align the specimen and the calorimeter on the rotating bearing. The desired flow conditions were then set and the calorimeter rotated into the flame to measure the heat flux as described previously. The sample to be tested was then rotated into the same position in the flame and the Honeywell recorder started. Samples were heated for seven to ten minutes depending on the depth of the thermocouples in a given specimen.

The data recorded for a typical run were oxygen and acetylene flow rates, oxygen and acetylene regulator pressures, sample position, thermocouple positions, and a continuous record of the thermal transients of each thermocouple. If three temperatures were to be measured, the recording pen which was monitoring the thermocouple nearest to the heated surface was switched to the last thermocouple once the temperature of the first thermocouple exceeded the range of the recorder. After completion of the test, the sample was allowed to cool and several were cut to determine the one-dimensionality of the recession of the impregnate.

CHAPTER V

RESULTS

Figure 10 depicts a schematic of a ceramic sample during the heating period. Regions A and B represent successive regions of the model for which individual analyses and measurements were required. Region A includes the region of mixing and axial decay of the subsonic, turbulent jet. Analysis of this region considered the mixing, decay, and chemistry of the experimental facility to yield the environmental enthalpy, velocity, and species to which region B is exposed. These results were available at successive axial positions, U, downstream from the jet exit.

Region A also includes the stagnation point boundary layer on the test material. It is in this aspect of the problem that the combined effects of environmental and injectant chemistry, mass addition into the boundary layer, and the transient response of the material impose significant coupling effects. Results for this region may be divided into two successive developments. The first yields information for the "cold-wall" heating environment at a specified axial position. The second yields the variations of these latter conditions due to the transient thermal response of the heated surface and mass injection as specified from the solution of region B.

Region B represents the region of solution for the transient thermal response of the heated material subject to the conditions

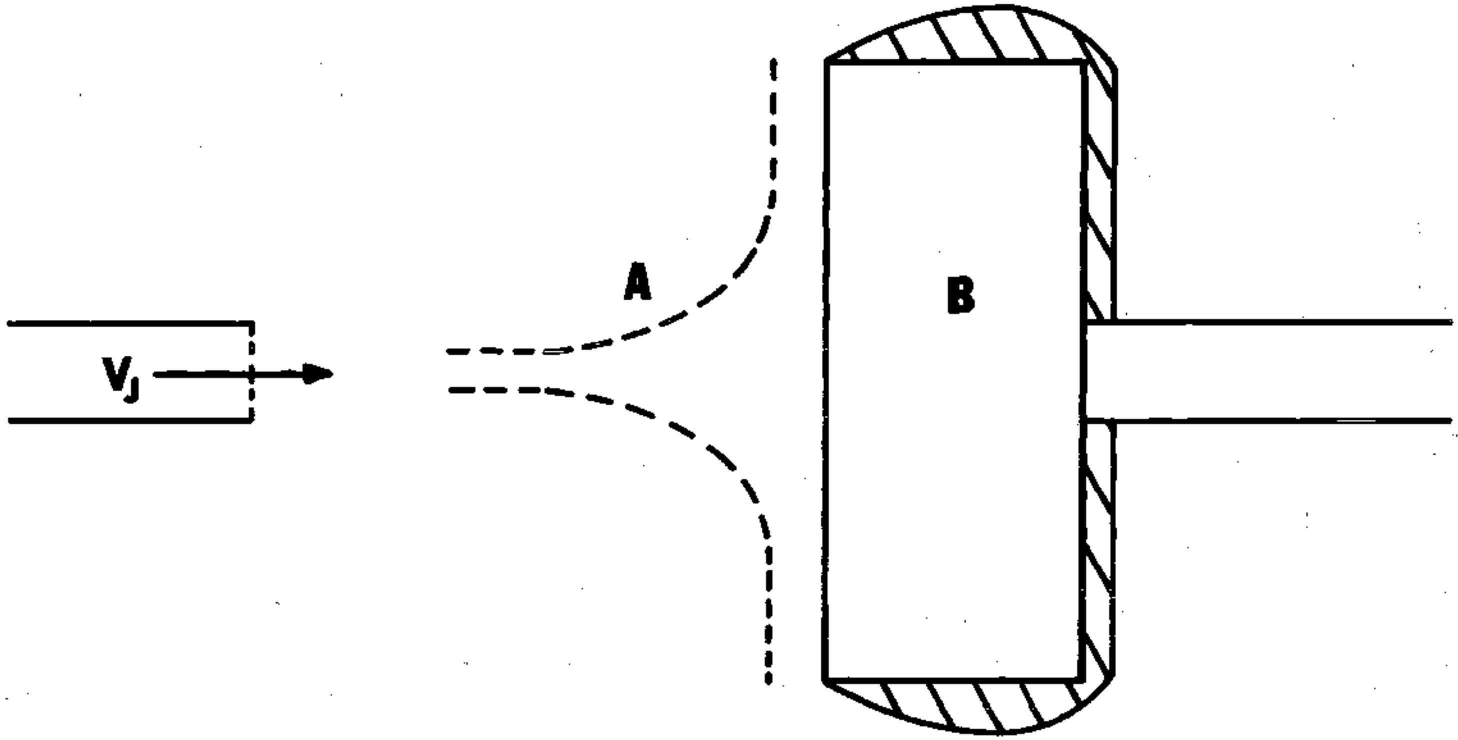

Figure 10. Oxy-acetylene Test Schematic

imposed with the coupling to the environment of A. The results from region A provide the heat flux boundary condition for the governing equations of B. Solution of these equations provide the basis for evaluation of the specified system and the relative contribution of the various phenomena to the total thermal protection. Results of the respective analyses will be presented in the order discussed above, leading successively to the final system evaluation.

Jet Mixing Results

The portion of this study devoted to the evaluation of region A required first the theoretical results of the turbulent mixing analysis to yield the property variations as a function of the center-line velocity decay.

Table 2 summarizes the jet exit and environmental conditions used in the analyses. The jet Reynolds number of 19,700 for 25 SCFH is approximately twice the value given by Hottel and Hawthorne (41) for laminar to turbulent transition. The jet velocities are mass average values calculated from the measured gas flow rates to the torch. Element and species jet concentrations are those resulting from the volumetric ratio of oxidizer to fuel of 1.2 recommended by ASTM (41). This restriction was applied to the tests for each of the three flow rates listed. Element mass fractions in the jet were therefore constant for all of the three flow rates considered.

The variation along the jet axis of element mass fractions and free stream species mass fractions are shown respectively in Figures 11, 12, and 13. Increasing values of U correspond to approaching

Table 2. Jet and Environmental Conditions

Re = 19,000	P = 14.7 psia	T_J = 1,000 R
	C_2H_2 Flow Rates	
15 SCFH	20 SCFH	25 SCFH
	Jet Velocity for above Flow Rates	
472 ft/sec	628 ft/sec	786 ft/sec
	Jet Mole Fractions	
C_2H_2 = 0.455	O_2 = 0.545	$N_{O_2}/N_{C_2H_2}$ = 1.2
	Jet Element Mass Fractions	
Carbon = .373	Hydrogen = 0.031	Oxygen = 0.596
Jet Enthalpy:	h = 1664.3 BTU/lbm	
Surrounding environment: atmospheric air at 100°F		
	Mass Fractions	
Oxygen = 0.232	Nitrogen = 0.768	
Enthalpy = 5.6 BTU/lbm		

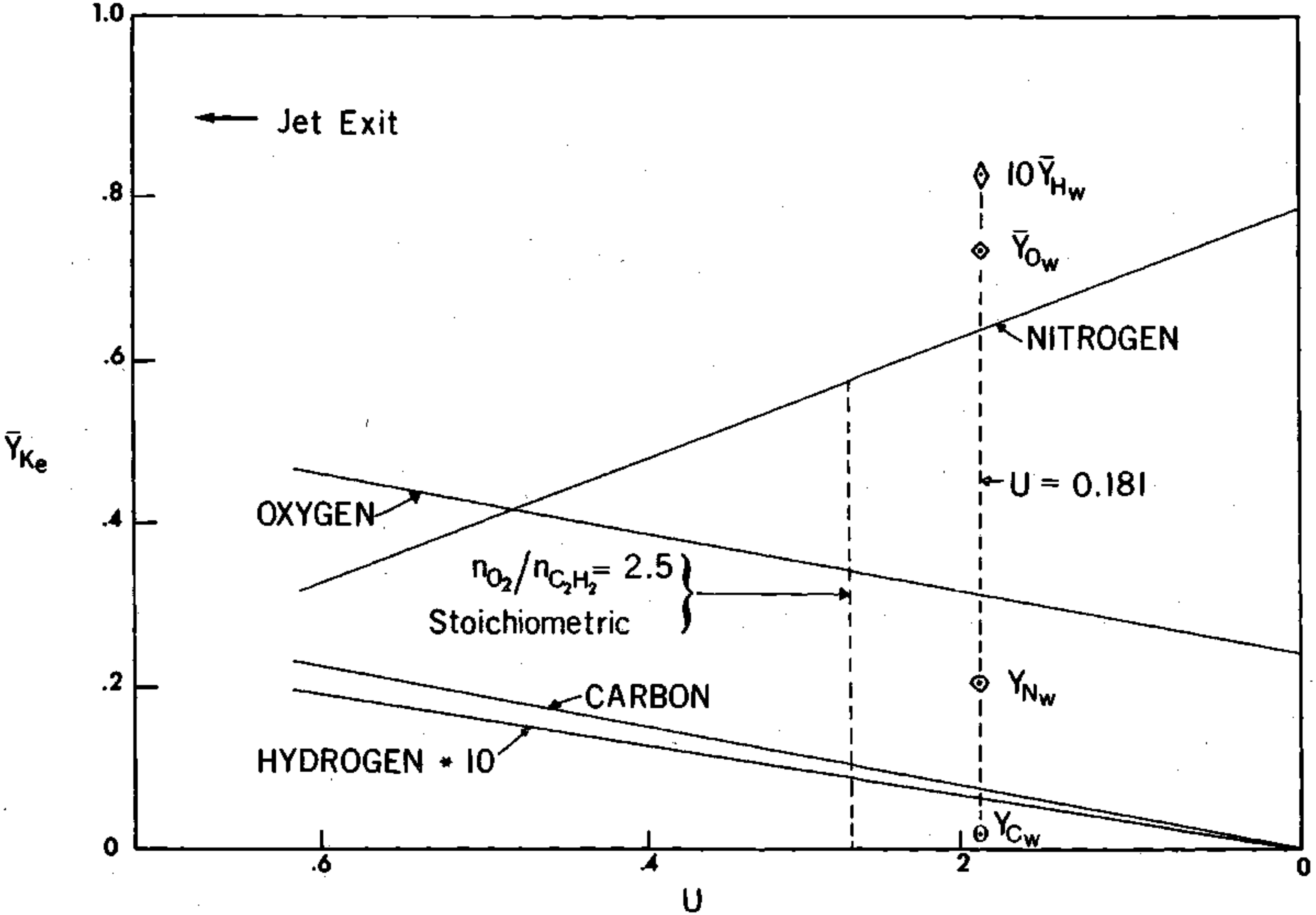

Figure 11. Mixing Region Element Mass Fraction Versus U

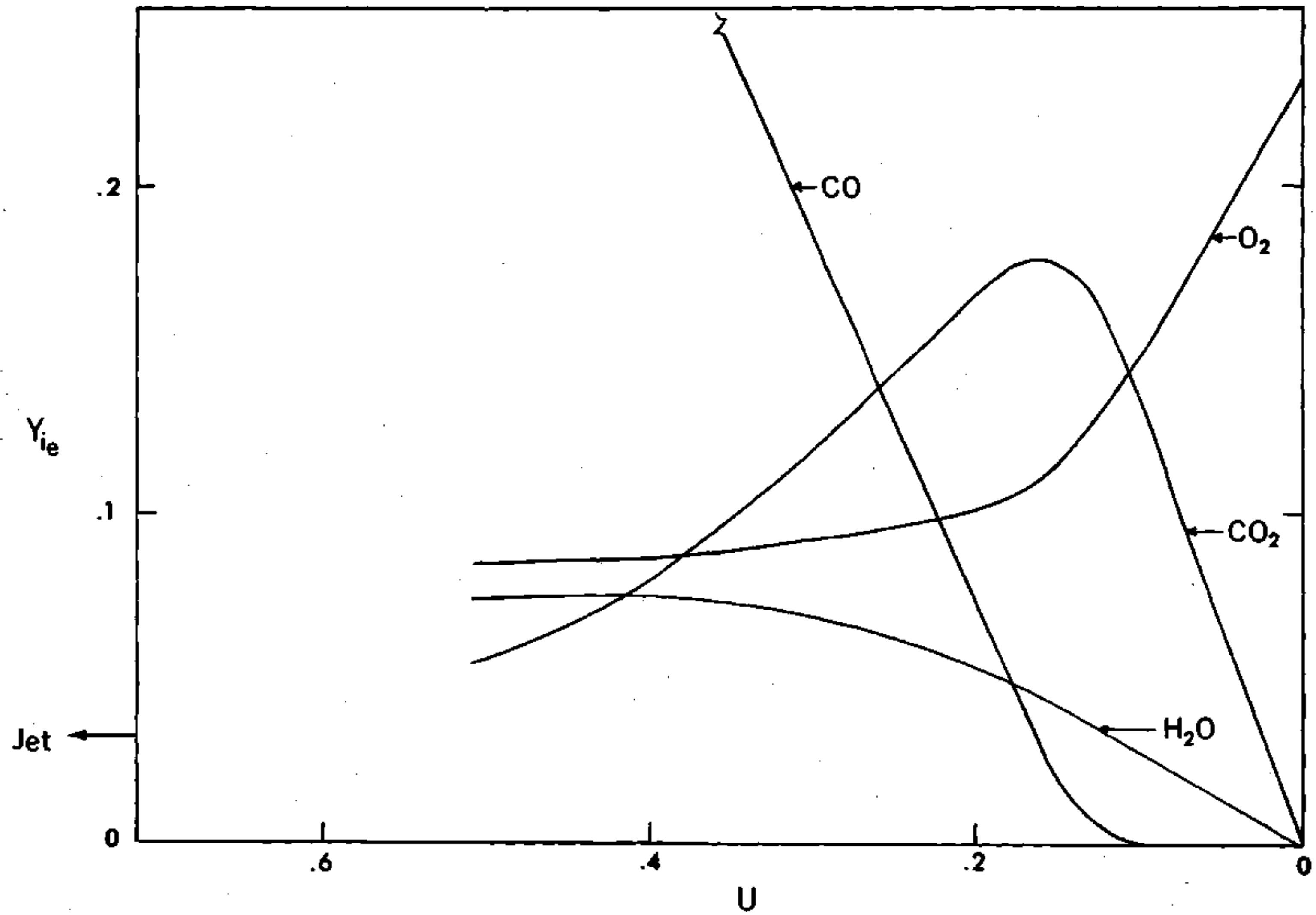

Figure 12. Species Free Stream Mass Fraction Versus U

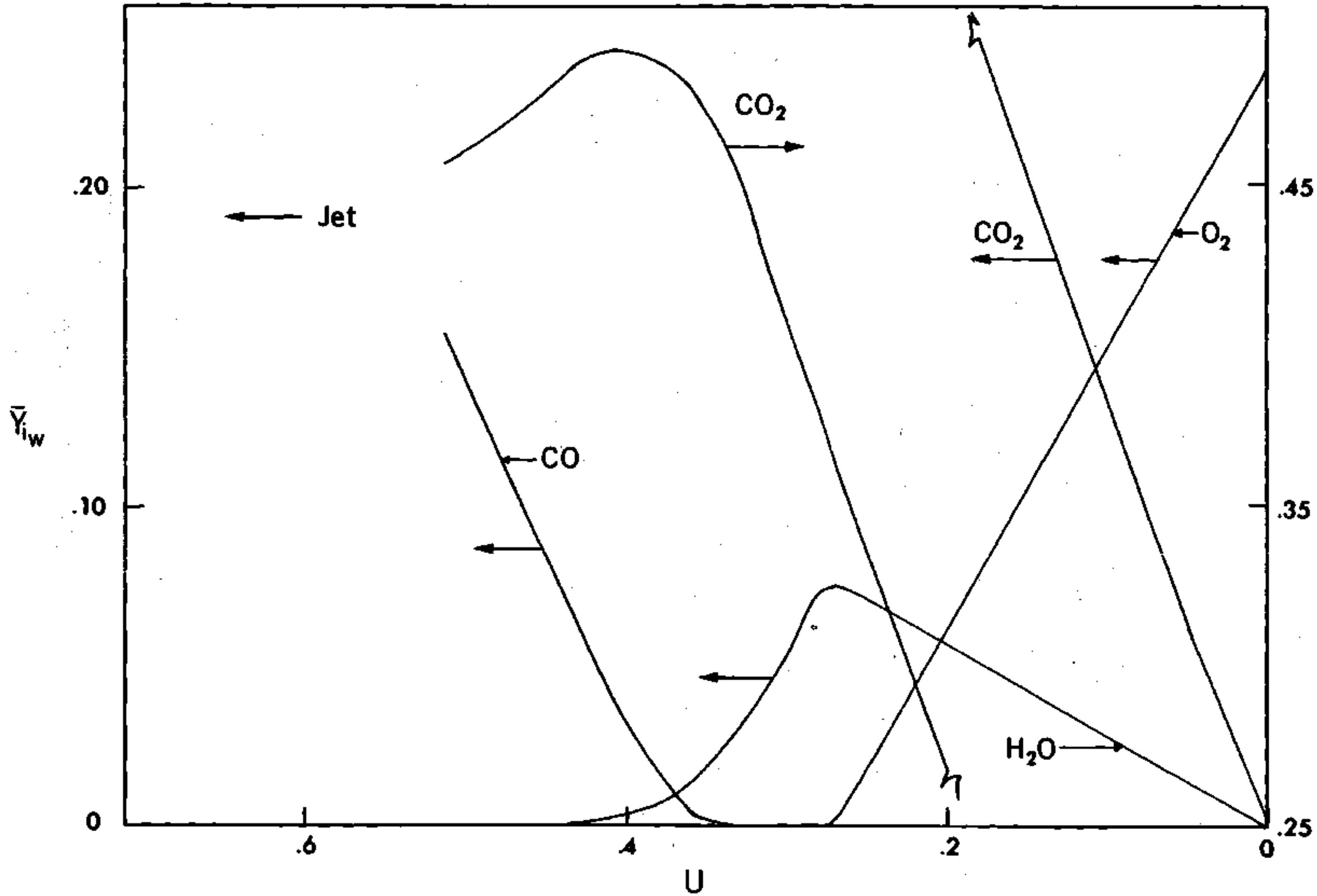

Figure 13. Surface Species Mass Fraction Versus U

the torch or jet exit. Results of Figure 11 also correspond to surface element mass fractions for zero injection. Changes in equilibrium composition indicated in Figure 12 are a result not only of the increase in flame temperature as the jet is approached, but also in the significant redistribution of element concentration shown in Figure 11 due to mixing. The U = 0.181 values correspond to the point at which the impregnated ceramic tests were performed. While the species concentrations of Figures 12 and 13 are important in calculating the transport and thermodynamic properties of the multi-component jet, it is the zero injection element mass fractions at the surface which are directly altered with boundary layer injection as seen by the dependence of equation 3.38 on f(0). Calculated surface element mass fractions for f(0) = -0.753 are also shown in Figure 11 to indicate the magnitude of the shift of element concentration due to surface injection. This also indicates the degree of coupling for results for surface chemistry on environmental conditions and injection rate. Thus variations in surface species chemistry result from the transient temperature rise <u>and</u> to the shift in element concentration with injection. As rates of injection decrease, the surface element concentrations will approach the zero injection values at specified test conditions. The rate at which the surface element concentrations approach the zero injection values with decreasing f(0) is linearly dependent upon free stream element concentration, $\overline{Y}_{ke}$ as can be seen by differentiation of equation 3.38. Through this dependency the specific environmental chemistry exhibits a significant effect on the rate of variation of surface heat transfer with injection rate, f(0).

It is noted that a stoichiometric ratio of oxygen to fuel theoretically occurs only at $U = 0.264$. At this point however the mass ratio of nitrogen to oxygen is approximately half that for air. Thus theoretically, exact stoichiometric conditions for air and C_2H_2 do not occur at any location along the jet axis.

It is seen from Figure 13 that the surface mass fraction of molecular oxygen is negligible for $U > 0.27$. At distances from the jet exit greater than this, $U < 0.27$, excess oxygen is available and would promote surface formation of CO_2 and H_2O which would tend to increase surface heat transfer as predicted by Lees (12). At locations closer to the jet exit, $U > 0.27$, excess oxygen is not available and a decreasing concentration of CO_2 and H_2O should result. Thus the indicated decreasing concentrations of water vapor and CO_2 and the increasing concentration of CO.

Figure 14 shows the predicted variation of freestream enthalpy and adiabatic flame temperature. These values are determined for the local species and element concentrations given in the previous figures.

Comments are in order concerning the magnitude of flame temperatures predicted. This analysis predicts a flame temperature of $2685^{\circ}K$ (4834 R) for stoichiometric conditions. This is approximately $70^{\circ}K$ above the maximum flame temperatures measured by Lewis and von Elbe (42) also for stoichiometric air/fuel ratios. As has been previously noted, a stoichiometric ratio of acetylene to oxygen theoretically occurs at $U = 0.264$. At this point the nitrogen to fuel ratio is 4.81 moles N_2/mole fuel, approximately half that of stoichiometric C_2H_2 - air with a predicted flame temperature of 5600 R. Gaydon (43)

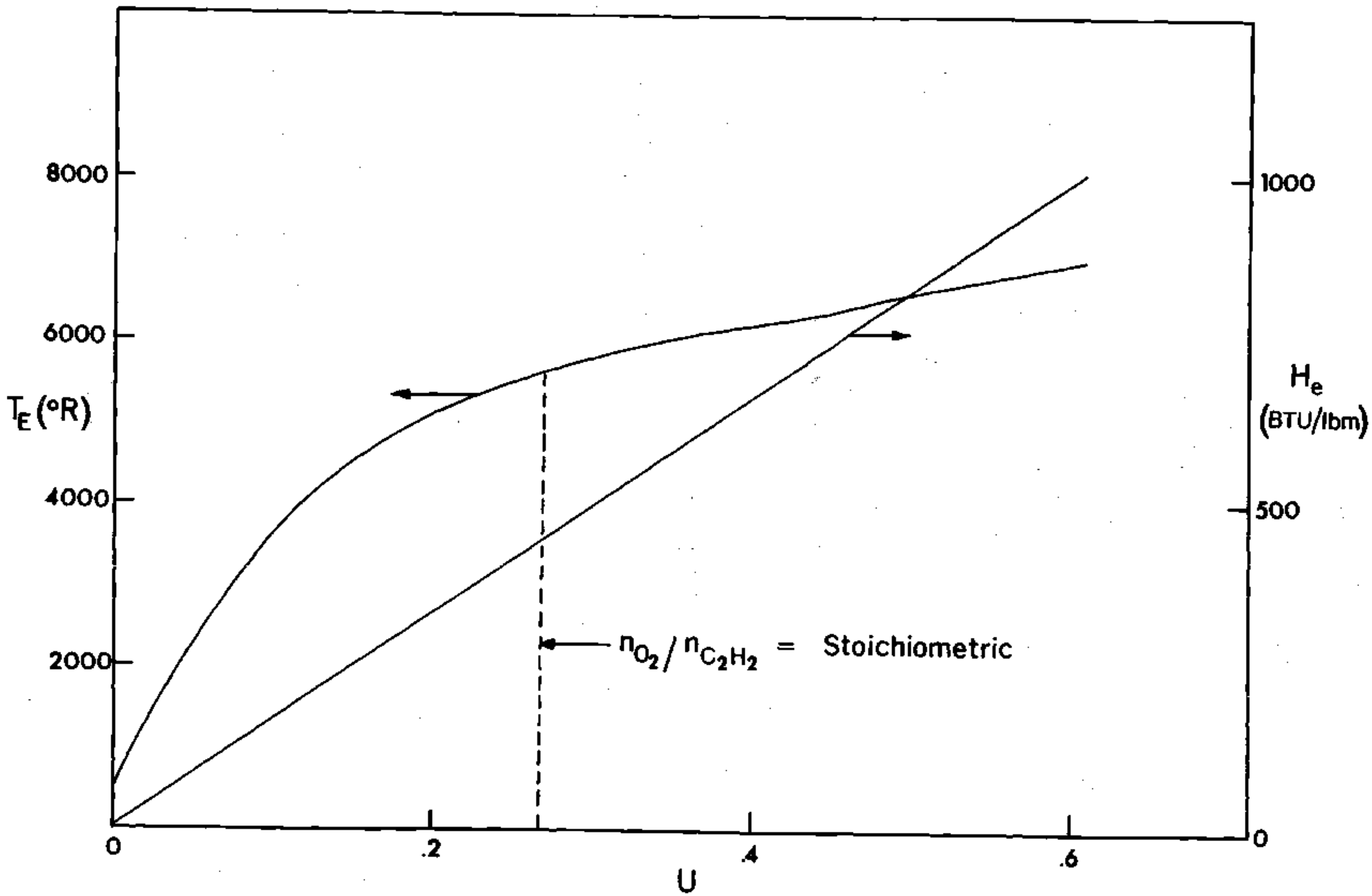

Figure 14. Adiabatic Flame Temperature and Stagnation Enthalpy Versus U

reported that the maximum flame temperatures for C_2H_2/O_2 combustion occur well to the rich side of stoichiometric. Gaydon further reports that the main chemical processes are normally completed in a very short time during passage through the reaction zone of the flame, but in some cases the chemical reactions are not complete. He further states that the luminous zone of the flame front coincides quite well with the reaction zone. Flames generally radiate strongly from this flame front or luminous zone with radiation beyond the flame front mainly from gases in chemical equilibrium. Bartholeme (44) predicts $3335^{\circ}K$(6000 R) for combustion with theoretical oxygen with a value of $3222^{\circ}K$(5800 R) with the addition of 1.07 moles N_2/mole fuel. While the information given above may seem to justify the magnitude of the entire range of temperature predictions, it is felt that these results are not valid within the proximity of the inner cone due to the incomplete oxidation of C_2H_2 in this region.

The final result of the analysis for region A is shown in Figure 15. The heat flux parameter presented in this manner is valid for various flow conditions needing only the stagnation point velocity gradient for the given surface to yield the cold-wall heat flux. For example, for the conditions of fuel/oxidizer ratio and chemical enthalpy given in Table 2, these results would be applicable for a wide range of jet flow rates and test surface configurations. The lower rate of increase in cold wall heat flux occurring approximately at $U = 0.25$ is directly attributable to the element chemistry variations along the axis. Figure 13 shows this to coincide with the depletion of the available oxygen and subsequent increase in carbon monoxide

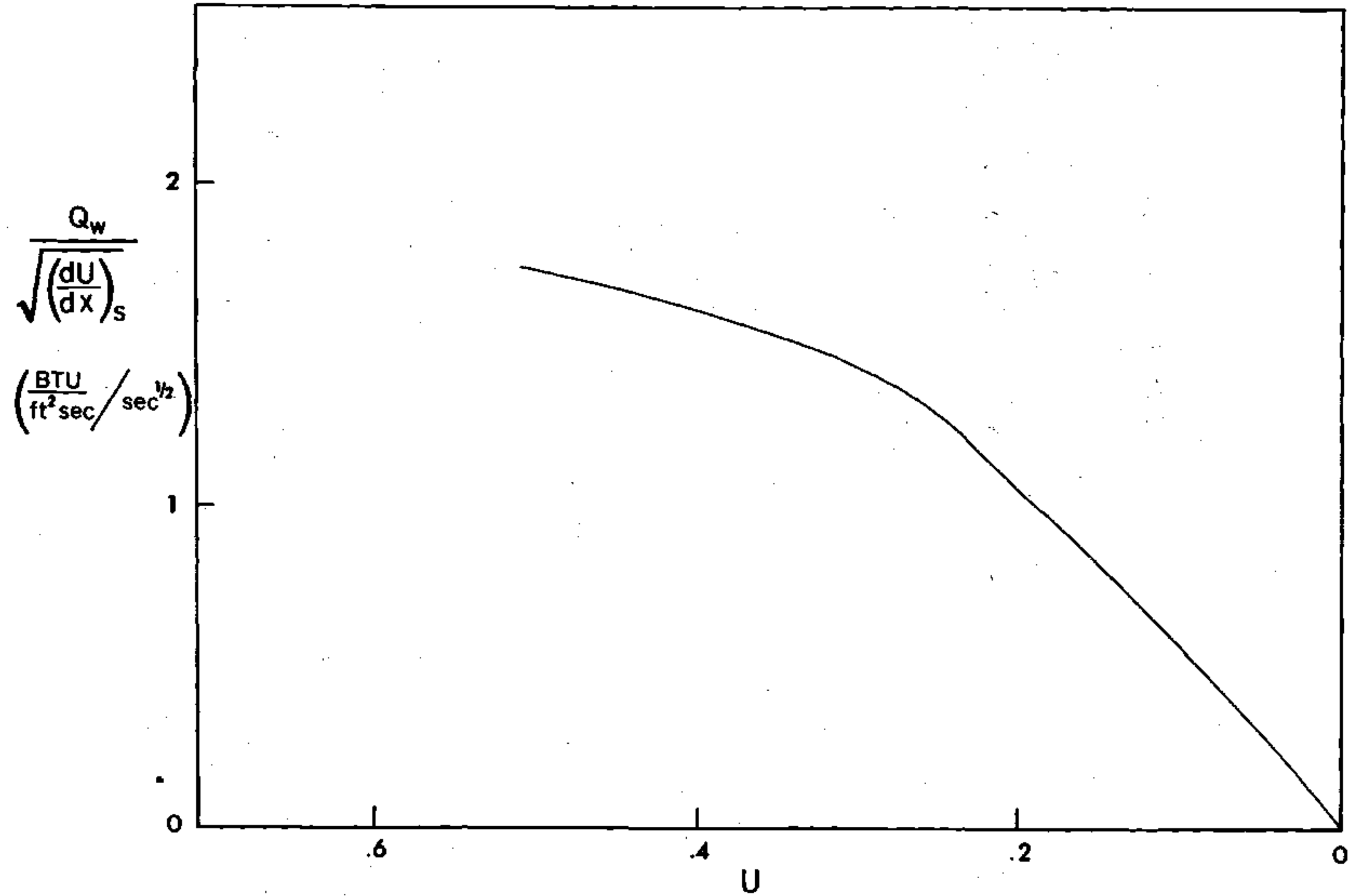

Figure 15. Cold - Wall Heat Transfer Parameter Versus U

formation as discussed previously. At this point the energy released due to exothermic surface recombination decreased which resulted in a lower rate of heat transfer increase. Experimental data exhibiting this effect will be discussed subsequently.

To be applicable to a given facility, information must be available as a function of the coordinate dimensions of the experimental facility. Figures 16 and 17 give the measured stagnation pressure and resultant centerline velocity decay for the three flow rates listed in Table 2. The velocities were calculated from Bernoulli's equation and the stagnation pressure measurements of Figure 16. A trial and error procedure was used to obtain the local gas density in the boundary layer. At any given position, a value of non-dimensional velocity, U, was assumed. The free stream density predicted from the mixing analysis of Chapter III was used to calculate the local gas velocity and its non-dimensional equivalent. Iteration continued until the assumed and calculated value of U were within 0.002. With these results, the specification of freestream chemistry, enthalpy, and heat flux at individual axial distances were known. It is noted that these measurements were made with the probe shown in Figure 7, but were applied to a jet at normal incidence on a flat plate. Snedeker and Donaldson (45) have compared axial stagnation pressure measurements for free and impinging jets under several flow conditions and surface geometries. Significant differences occur in stagnation pressure measurement for free and impinging jets for underexpanded, supersonic conditions at the jet exit. However, no differences are observed in the data for stagnation pressure of a free subsonic jet and the same

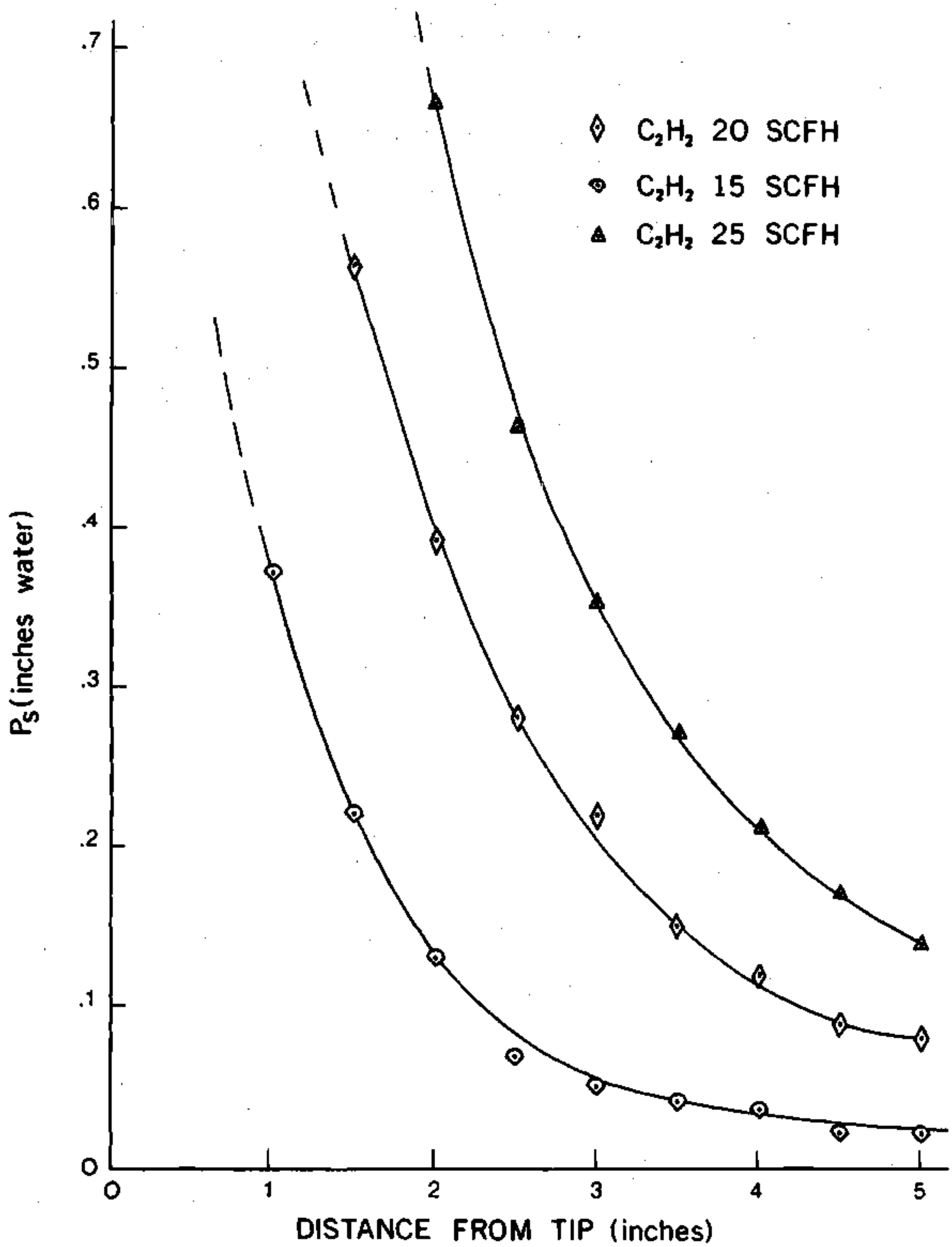

Figure 16. Stagnation Pressure Decay Along Jet Axis

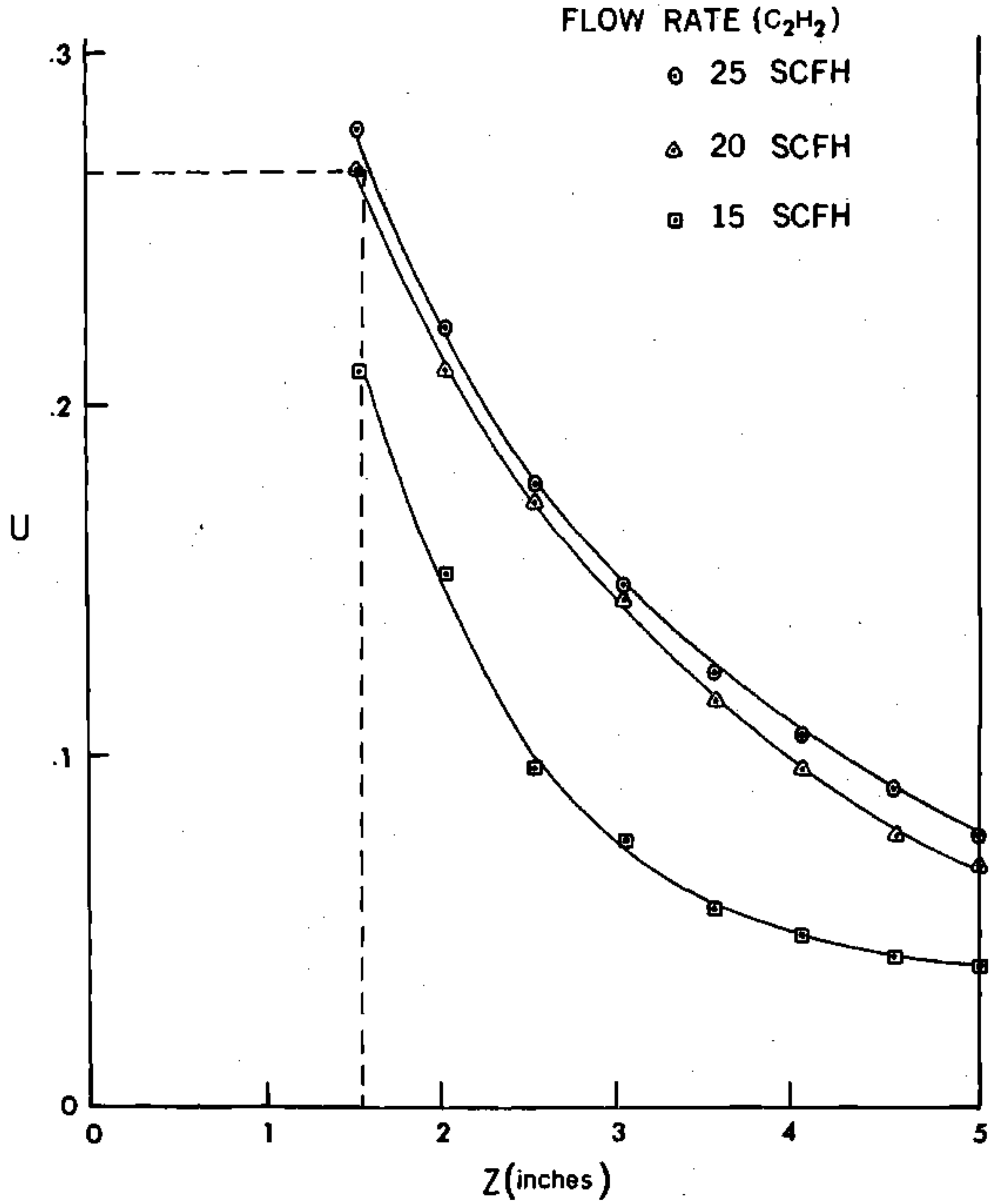

Figure 17. Axial Velocity Decay Along Jet Axis

jet at normal incidence on a flat plate. It is noted however that radial variations (and therefore the stagnation point velocity gradient) are dependent upon the shape of the given surface.

Figure 17 would indicate that the location of the position for stoichiometric fuel/oxygen ratio to be approximately 1.5 inches, where $U = 0.264$. As discussed earlier, the experimental maximum flame temperatures are reported to occur for fuel rich conditions and approximately at the end of the reaction zone. The length of the inner cone was observed to be approximately one inch in length which would correspond to $U = 0.35$ (Figure 17). The calculated flame temperature for this condition is $5970^{\circ}R$ ($3260^{\circ}K$). This compares very favorably with measurements of $3200^{\circ}K$ reported by Gaydon (43) 1mm above the reaction zone, and does occur at a significantly richer fuel/oxidizer ratio than that of stiochiometric. From Figure 17, the one inch length of the inner cone corresponds to $U = .35$. Assuming, as discussed previously, that this corresponds approximately to the edge of the reaction zone, the results of the mixing analysis for flame temperature, species mass fractions, and heat flux were restricted to distances greater than one inch from the jet exit, i.e., $U < 0.35$. Past this location, the successive reactions to complete the fuel oxidation are still occurring and local equilibrium would not be a valid assumption. However Lewis and von Elbe (42) report that once transition from laminar to turbulent jet flow occurs, the length of the inner cone remains essentially constant. Thus test locations of magnitudes greater than 0.35 could be obtained outside the reaction zone by increasing the flow rate and shifting the location of a given value of U of Figure 17 further to the right.

Figure 18 shows the results of the cold-wall heat flux measurements in the oxy-acetylene facility. Each of the curves exhibit a decreasing slope as the jet is approached. A similar result was predicted theoretically in Figure 15 due to surface chemistry effects resulting from depletion of the available oxygen.

The results for the heat flux parameter shown in Figure 15 were used with the heat flux measurements to calculate the stagnation point velocity gradient. This was used in the definition of f(0), equation 3.33, which in turn was used to evaluate the dimensionless wall gradients, π_T' and π_{AB}', and to calculate the surface element mass fractions from equation 3.38.

At the test location of 2.5 inches, U = .181, the stagnation point velocity gradient was calculated to be 25,680 sec^{-1}. Comfort, (46) reports a stagnation point velocity gradient of 9600 sec^{-1} at the same number of jet diameters from the exit of a subsonic, arc heated nitrogen jet. Snedeker and Donaldson (45) predict a value of 11,100 sec^{-1} at an equivalent position for a jet Reynolds number of 147,000.

The data and predictions of the previous section were used to specify the initial cold-wall thermal and chemical environment to which test specimens were exposed at a specified location. The tests performed on the porous, impregnated slabs were at a distance of 2.5 inches from the jet exit with an acetylene flow rate of 25 SCFH. Table 3 summarizes the measured and calculated conditions required to specify the thermal and chemical environment at this test condition. Substitution of the above data in the analysis of Chapter III

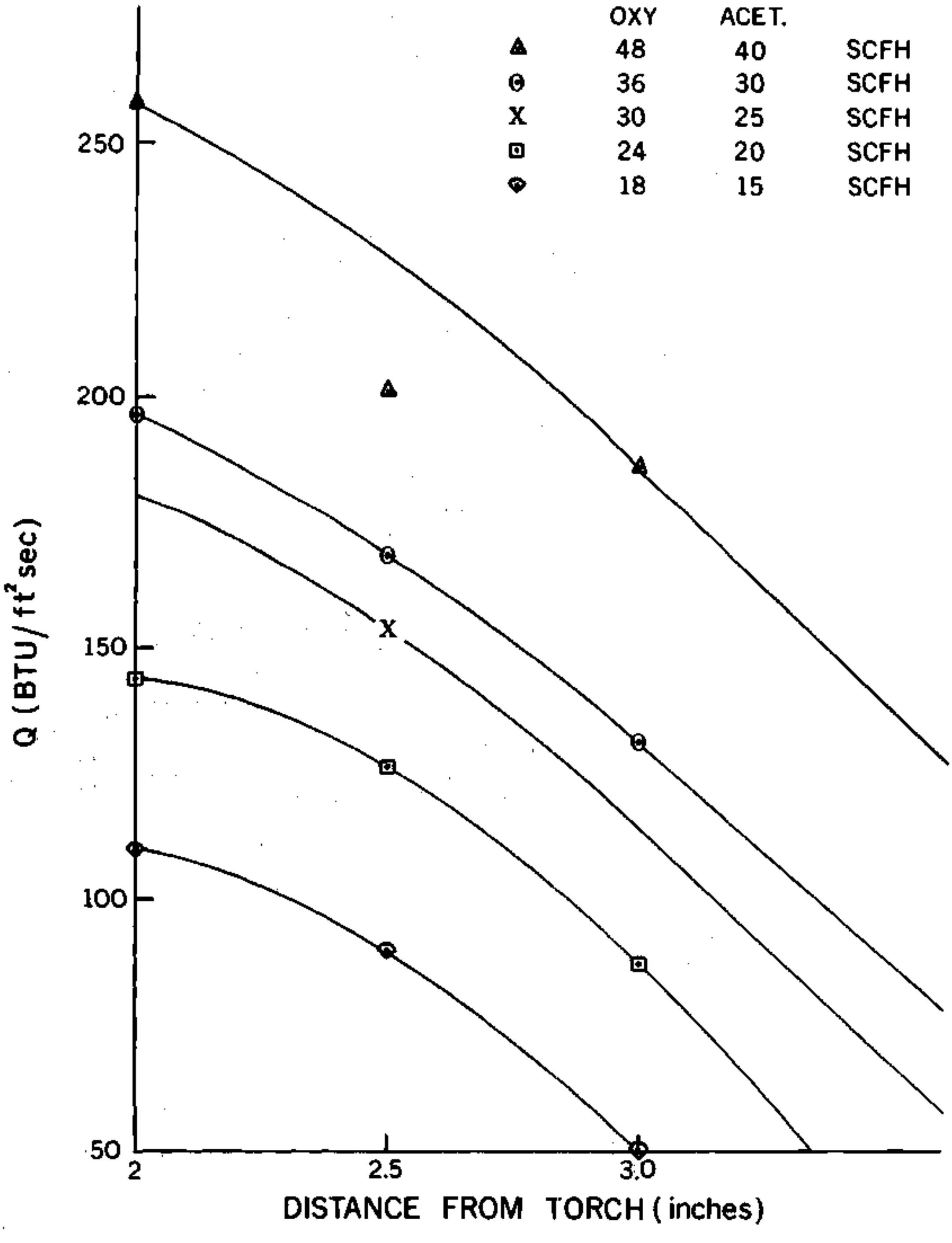

Figure 18. Stagnation Heat Transfer along Jet Axis

Table 3. Test Location Conditions

Fuel Flow Rate = 25 SCFH	Axial Position = 2.5"	$U = 0.181$
Stagnation Enthalpy = 308.6 BTU/lbm	Cold Wall Enthalpy = -1213.8 BTU/lbm	
Cold Wall Heat Flux: q_o = 150 BTU/ft^{2}sec	$\frac{dU}{ds}$ = 25680 1/sec	Pr = 0.77
Te = 4977°R	ρ_e = .0081 lbm/ft^3	μ_e=5.31*10^{-5}lbm/ft.sec.

Free Stream Element Mass Fractions

Carbon = .0675	Oxygen = .298	Nitrogen = .629	Hydrogen = .0056

Average slab thickness = 0.90 inches

Initial temperature = 50°F

provided the boundary conditions for the transient heating of the porous, impregnated system.

Thermal Response of Hydrated Systems

The most readily identifiable experimental phenomena measured during the transient heating tests was the variation of the interface position in the porous slab during the heating tests. Results shown in Figure 19 correspond to test conditions specified in Table 3. It is seen that approximately 700 seconds was required for the interface to recede completely through the porous matrix. The rate of recession was most rapid initially with the interface closest to the heated surface. The interface velocity gradually decreases, reaching a fairly constant value for the last 300 seconds of the test. The theoretical prediction of the interface recession is seen to lag experimental results during the latter phase of the tests. An error in location of the thermocouples is one possible source of this difference. It is estimated the thermocouple placements were accurate to within 0.05 inches. An error band of this width around the theoretical results would include all but four data points. A second possible source of error was incomplete impregnation of the porous matrix with the gel. Silica cement was placed on all surfaces of the samples except the heated surface before the gelatine was impregnated in the porous matrix. This would be equivalent to lowering the effective void volume of the sample and would decrease measured response time. Equation 3.10 would then predict an increased interface velocity. It will be seen later in this section that this would also decrease the

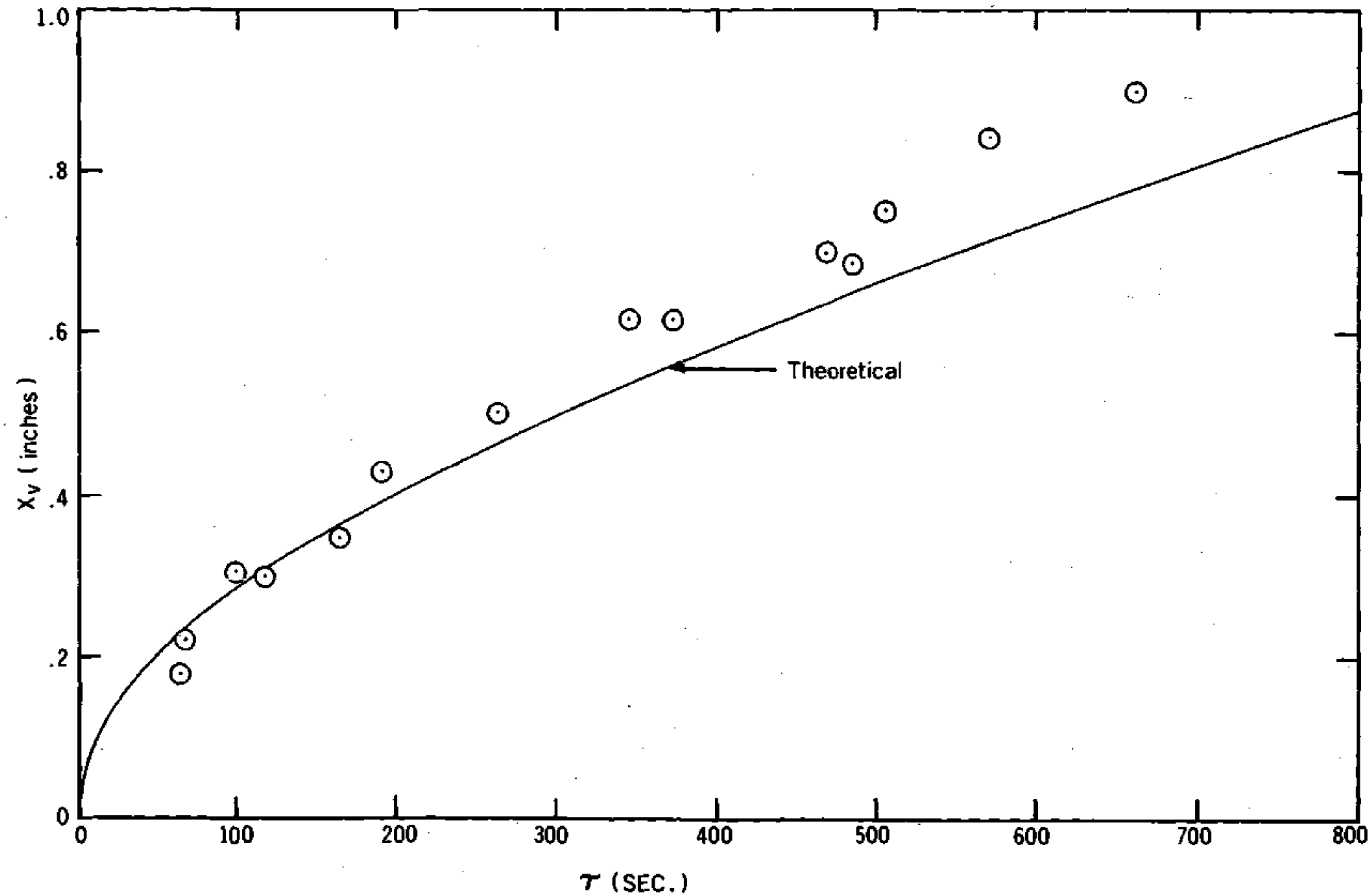

Figure 19. Interface Position Versus Time $q_{cw} = 150$ BTU/ft^2-sec

relative contribution of two phenomena which account for approximately 70 percent of the energy transferred into the sample from the environment. It is noted that the times used for the experimental data were those values indicated by the passing of the heated side of the interface past the thermocouple location. This can be seen in Figure 20 which presents typical test results from a thermocouple located 0.625 inches from the heated surface. A definite isothermal period was indicated corresponding to the passage of the interface of finite thickness past this position in the slab. Similar results were obtained for all test locations with the duration of the isothermal period being the shortest when the interface was nearest the heated surface and gradually increasing as it receded. These isothermal periods ranged in duration from 16 to 220 seconds as indicated in Table 4. The latter value would seen to indicate an interface of considerable thickness during the latter portions of the tests. A thickness was calculated from these times based on the interface velocity predicted from equation 3.10. This predicted an interface thickness ranging from 0.03 to 0.16 inches as seen in Table 5. The largest contributing factor to this apparent interface thickness was the small backside temperature gradient during the last 200 seconds of testing. Theoretical results predict a maximum drop of less than one degree between the interface and the insulated surface during the above period. As this was within the 1°F sensitivity of the recorder, it was impossible to record any variation during this period. The rapid rise in temperature observed with the passage of the interface would indicate that the heated side was easily defined experimentally. This was important

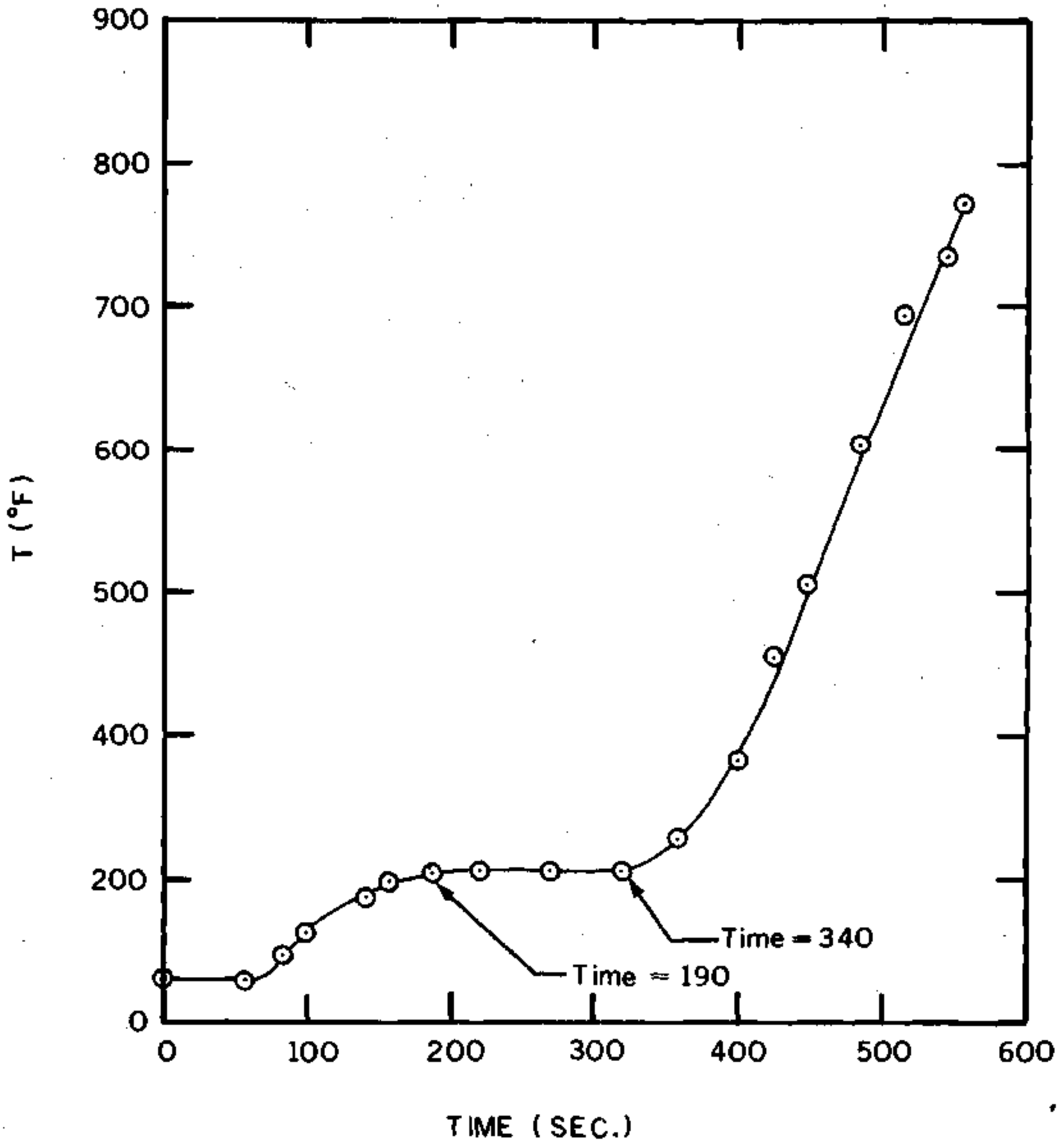

Figure 20. Measured Transient Temperature Response at X = 0.625 inches

Table 4. Experimental Interface Data

Position (inches)	Time 1 (sec)	Time 2 (sec)
.219	55	68
.43	150	187
.31	65	98
.625	190	345
.85	310	570
.18	56	67
.50		261
.31	70	100
.625	226	373
.90	440	660
.69	255	485
.75	350	505
.625	170	340
.70	305	465
.30	90	117
.75	350	500

Table 5. Predicted Interface Thickness

Location (inches)	Time (sec)	Avg. Velocity (in./sec)	Zone Thickness (inches)
0.185	16	2.04 10^{-3}	0.03
0.35	42	1.35 10^{-3}	0.06
0.437	81	1.13 10^{-3}	0.091
0.625	147	0.98 10^{-3}	0.144
0.90	220	0.75 10^{-3}	0.16

theoretically as the temperature gradients on this side were the largest and dominated in the calculation of interface velocity and vaporization rate. It was the importance of interface velocity and vaporization rate in the coupling aspects of the problem which led to the use of the reference frame relative to the interface position for the theoretical analysis. Temperature profiles in the slab are shown in Figure 21. Backside temperature gradients are seen to be generally small in comparison with those from the heated surface as observed above. It is also seen that the surface temperature rise is small after the first 200 seconds. Past this point in the heating period the analysis did not predict any significant decrease in surface heat flux due to "hot-wall" effects. Surface chemistry and injection rates accounted for changes in surface heat transfer past this time.

It was observed in Chapter III that the thermal protection afforded by a transpiration cooled system is a result of surface heat transfer reductions due to hot wall and mass addition phenomena, surface chemistry effects, and internal energy transfers to the interface and evolved gases as well as to the solid matrix. To put these various phenomena in perspective, consider the test conditions listed in Table 3 for a total heating time of 750 seconds. The maximum cold wall heat transfer during this period was calculated to be 102,500 Btu/ft^2. The theoretical analysis of Chapter III predicted a net heat transfer to the porous matrix of approximately 9,800 Btu/ft^2 for a comparable test period. The reduction below the cold-wall value was due to the combined effects of mass addition, surface chemistry and the increase in surface temperature. The major reduction in

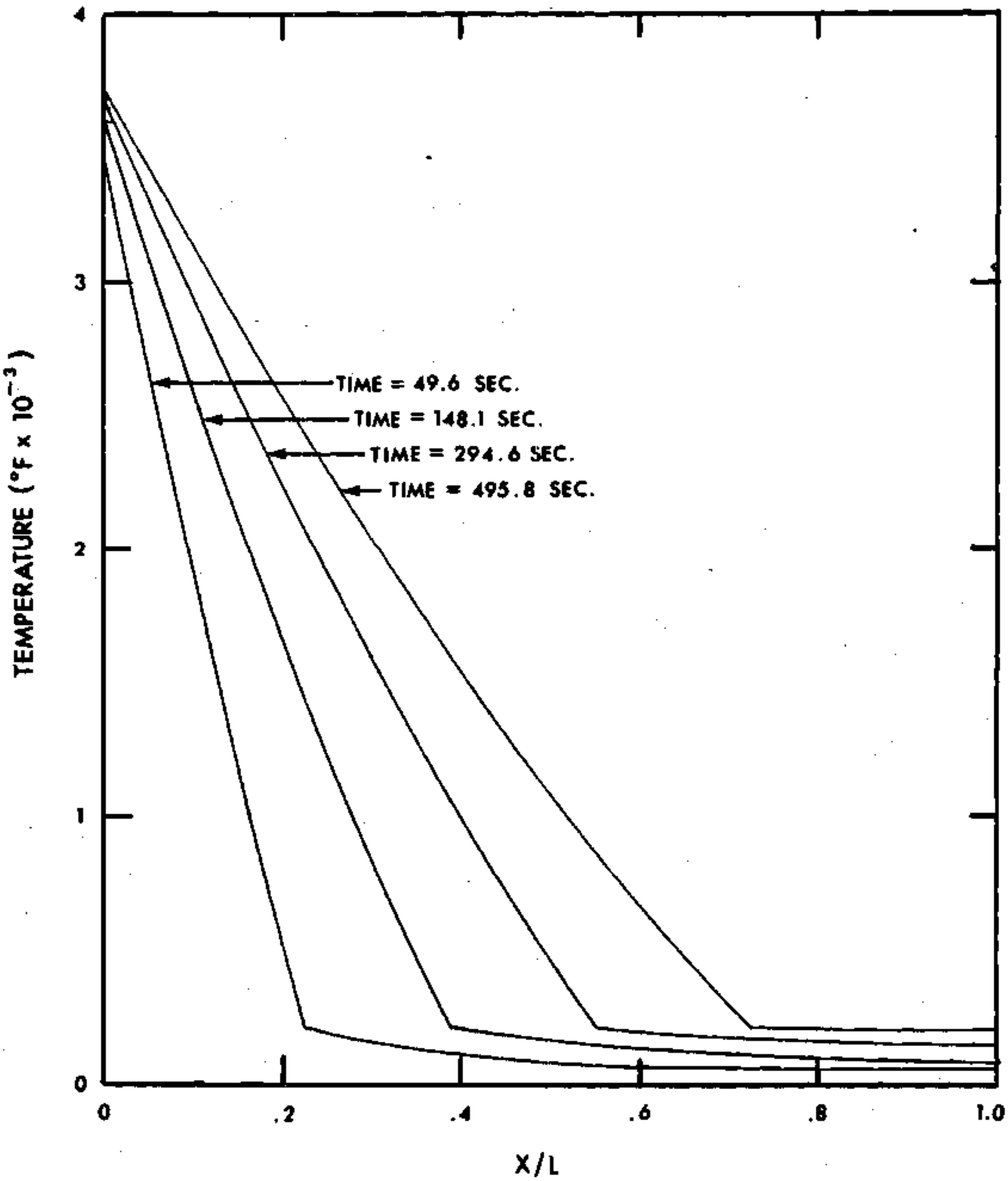

Figure 21. Transient Temperature Profiles for an Impregnated Slab

surface heat transfer was due to the increase in surface temperature from the initial cold-wall value. The predicted free stream to surface temperature difference dropped from over 4000°F to under 1000°F for the period of testing. The blowing effect was small, being no more than four percent relative to the zero-injection value at any time after 100 seconds. Surface chemistry contributions occur from the terms given below from equation 3.17. These terms

$$\rho D_{12} \Sigma hi_w \frac{\partial Y_i}{\partial y} - \rho v)_w \,(hw - hs) \tag{5.1}$$

were computed in the analysis with the net result that they contributed to an increase in heat transfer. The latter term was positive, decreasing the heat transfer as a result of a small degree of dissociation of the injected water vapor across the surface. It is noted that this dissociation was mainly due to a shift in element concentration across the surface with the presence of carbon and nitrogen at the gas boundary. From Table 3 the zero-injection surface element mass fractions were $\overline{Y}_c = .0675$, $\overline{Y}_o = .2979$, $\overline{Y}_N = .629$, and $\overline{Y}_H = .00566$. The predicted surface element mass fractions calculated from theoretical injection rates are shown in Figure 22. This is basically surface dissociation as a result of foreign gas injection into the boundary layer. Dissociation was neglected in the porous matrix. This was considered in a student report by Hopkins (47) directed by this author. An analysis was made of the contribution of dissociation of water vapor to the energy

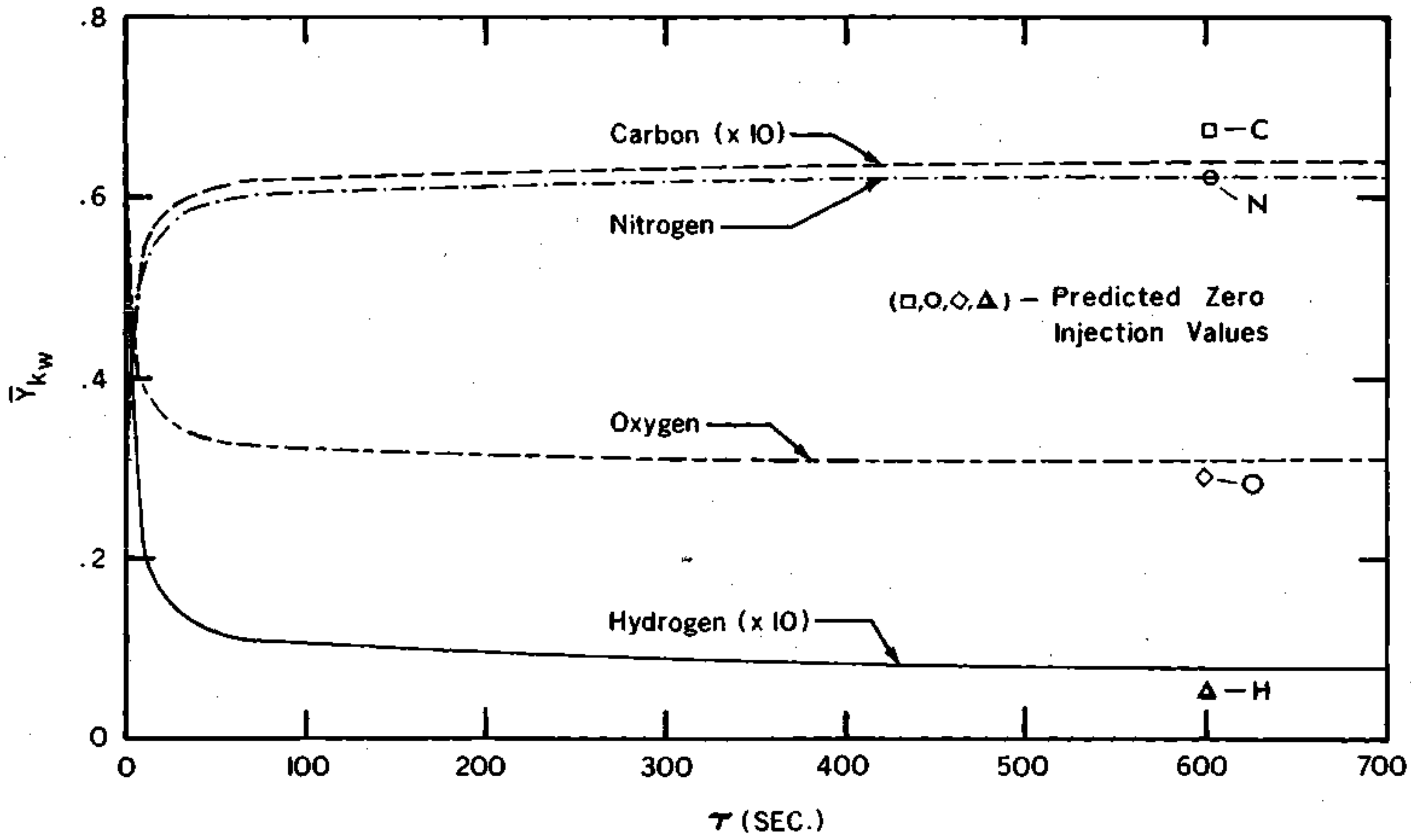

Figure 22. Variation of Surface Element Mass Fractions

transfer through a porous ceramic with transpiration cooling. The analysis showed that dissociation of water vapor was less than 2 percent below $4000^{\circ}R$. This resulted in an increased reduction of energy transfer of less than 5 percent relative to no dissociation or of less than 1 percent of q_o at a flow rate of 0.006 $lbm/ft^2 sec$. It is noted that the predicted vapor flow rate for this study was less than this value for times greater than 40 seconds.

The first term of 5.1 is also positive and tends to increase surface heat flux. The free stream surface concentration difference generally indicates diffusion of CO, O_2, and H_2 to the surface and diffusion of CO_2 and H_2O from the surface. This would indicate an energy contribution due to surface recombination to CO_2 and H_2O. The largest contribution in the summation is by the CO_2 diffusion. This effect would be absent in a standard atmosphere environment and would tend to reduce the surface heat flux. The absence in the free stream of any appreciable free hydrogen would also minimize any recombination of H_2O. Figure 23 shows the theoretical variation of each of these terms normalized with respect to the initial cold-wall heat flux. While the net difference between these two contributions ranges from one to four percent of q_o, when compared to the actual transient values of surface heat transfer, the contribution is significant. The difference between the two terms decreases with time which results in a decrease in the surface heat transfer. It is also noted that for the test conditions of the cold wall calorimeter, the latter term of equation 5.1 was identically zero for no mass addition while the former contributes 22 Btu/ft^2 sec or 14 percent to the cold wall heat

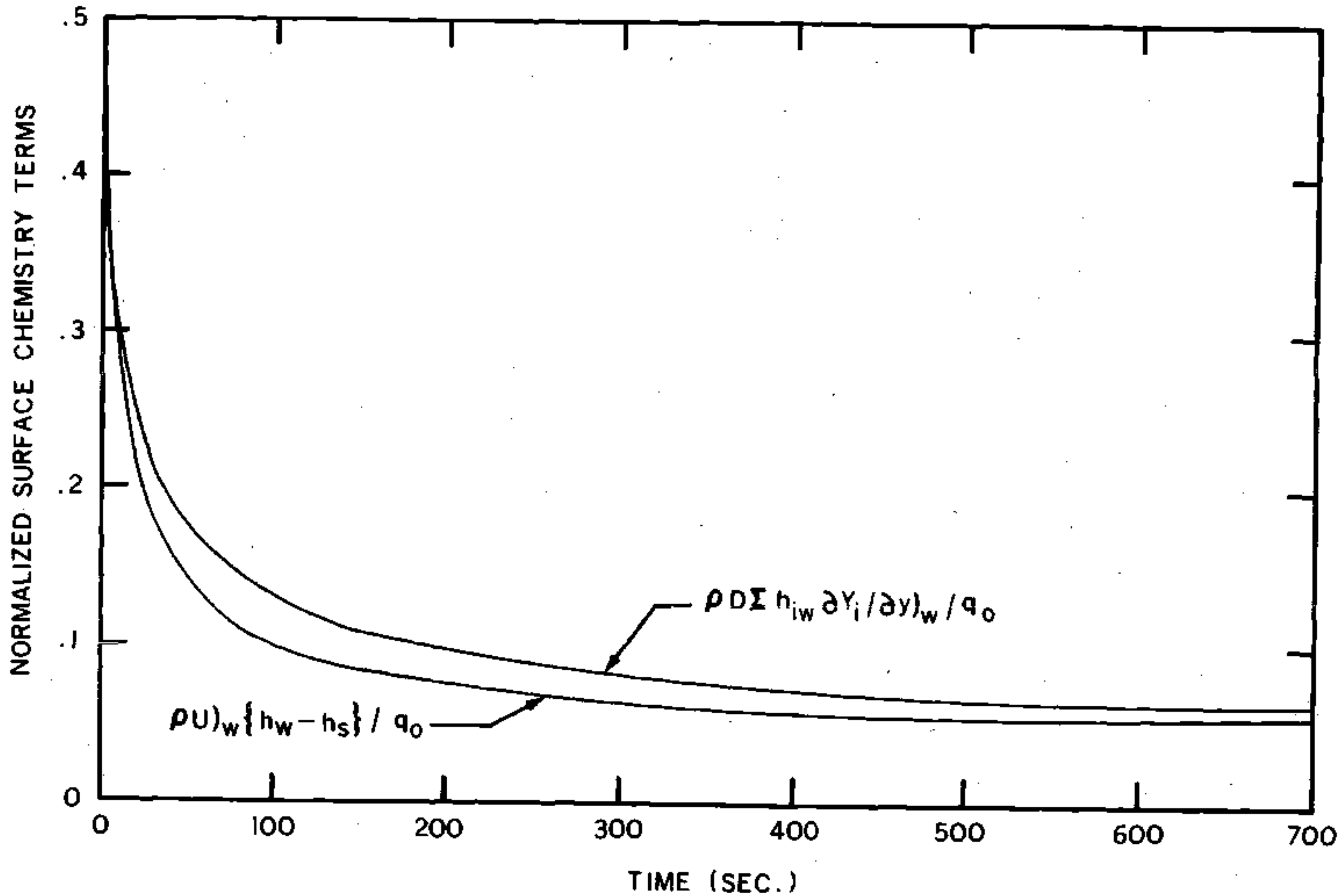

Figure 23. Normalized Surface Chemistry Contributions Versus Time

flux.

The remainder of the surface heat transfer was transmitted internally to the porous matrix. For a system with surface phase changes, most of the 9,800 Btu/ft^2 transferred to the slab would go into effective heat of vaporization at the gas-solid interface. However for the porous-impregnated system, this energy goes into stored energy of the solid matrix, interface vaporization and the heat capacity of the evolved gases between the interface and surface temperatures. The contribution of these latter two phenomena can be formulated as follows:

$$E_I\ (\tau) = \int_0^\tau \dot{m}_v\ \Delta h_v\ d\tau \tag{5.2}$$

$$E_v\ (\tau) = \int_0^\tau \dot{m}_v(\tau) \int_{T_v}^{T_s(\tau)} C_{P_v}\ dT\ d\tau \tag{5.3}$$

E_v, the energy required in heating the interface gases, accounts for approximately 50 percent of the surface heat transfer transmitted into the system as seen in Figure 24. Interface vaporization accounts for 20 percent with the remainder going to internal heat capacity of the solid matrix. Thus specific heat of the gases released by an impregnate is possibly a more important property than effective heat of vaporization in optimizing thermal protection for a transpiration

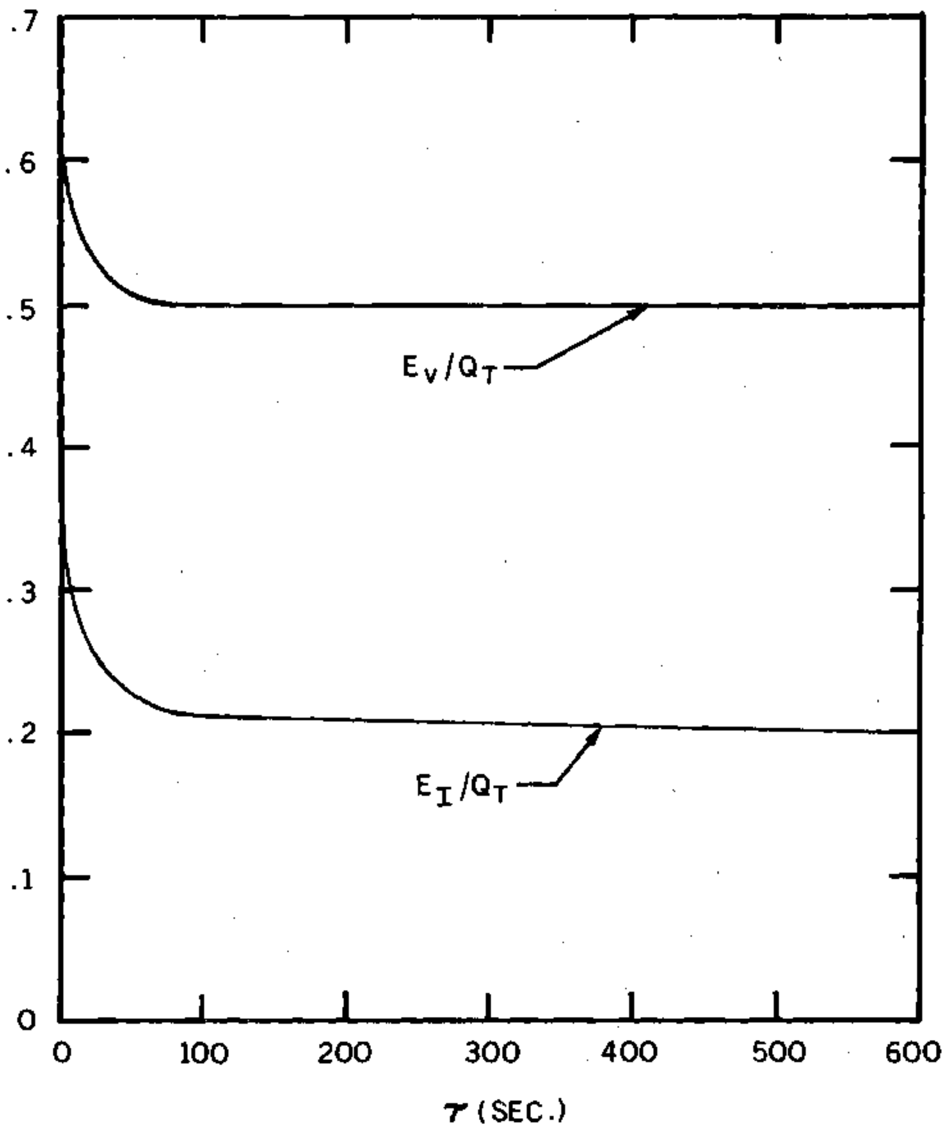

Figure 24. Non-dimensional Energy Contributions for the Impregnate

cooled system. For cases where the surface temperature rose rapidly initially and then remained fairly constant, an estimation of the relative contribution of these two terms could be made from equation 5.4.

$$E_v/E_T \cong C_{P_v}(Ts - Tv)/\Delta hv \tag{5.4}$$

This ratio was calculated to be 2.02 using a surface temperature of 3700°F and an average vapor specific heat of 0.56 BTU/lbm F. This compares favorably with a value of 2.5 calculated from the results of equations 5.2 and 5.3.

To determine the effects of environmental chemistry in this test facility, two variations of the analysis of Chapter III were programmed and computed for the boundary conditions listed in Table 3. One analysis assumed the surface element mass fractions were constant, but included mass addition effects on wall gradients, surface radiation and equilibrium chemistry changes with surface temperature. By differentiating equation 3.41 with respect to f(0), it is seen that this approximation is approached as f(0) approaches zero or as ϕ_K approaches $\overline{Y}_{Ke}$. The latter condition is the effect of foreign gas injection. The second analysis assumed the surface species mass fractions were constant at the cold-wall, zero injection value. Thus effects of the shift of element distribution and changes in surface temperature were neglected in the equilibrium chemistry calculation at the surface.

The results of these calculations are presented in Table 6 along with a summary of results from the analysis of Chapter III. The most significant effect was the reduction of the net contribution of the surface chemistry terms from equation 5.1. This resulted in a reduction in the total heat flux and surface temperature. The reduced surface temperature also lowered the relative importance of heat capacity of the impregnate vapor as compared to effective heat of vaporization of the interface. In comparing the first and last columns, the total heat flux was reduced 5.3 percent with the result that the time required for the interface to reach a depth of 0.95L was increased by 3.1 percent.

To further evaluate the importance of environmental chemistry in the oxy-acetylene facility, the analysis of Chapter III was applied for environmental conditions predicted at U = 0.10 and U = 0.30. Boundary conditions and thermodynamic property data required for these calculations were obtained from results presented in Figures 11 through 15. As the calculated cold-wall heat flux was different at each of these locations, the results shown in Table 7 are presented relative to the local Q_o or $\int_o^\tau q_o d\tau$.

As the torch tip was approached, cold-wall and surface heat flux increased and the time for the interface to recede to 0.95 L decreased. The time decrease was expected due to the increased heating rate, however the net contribution of the surface chemistry terms was also seen to increase with U. This is due to increased surface recombination with the free stream presence of H_2 and CO. It would

Table 6. Comparison Of Results to Point Where $X_V/L = .95$ at $U = .181$

	CONSTANT $\bar{Y}_{kw} = \bar{Y}_{kE}$	CONSTANT $Y_{iw} = Y_{iw_o}$	EQUILIBRIUM CHEMISTRY
$\rho D \sum h_{iw} \partial Y_i / \partial y)_w / q_o$	.125	.139	.158
$\rho v)_w (h_w - h_s) / q_o$	.038	.038	.0378
$\int_0^\tau q_s(\tau)\, d\tau$ (BTU/ft^2)	9,700	9,810	10,250
$\int_0^\tau \dot{m}_v(\tau)(h_s - h_v)\, d\tau$ (BTU/ft^2)	4,600	4,600	5,015
$\int_0^\tau \dot{m}_v(\tau)\, \Delta h_v\, d\tau$ (BTU/ft^2)	2,494	2,494	2,494
Time (τ) at $X_v/L = .95$ (sec.)	835	829	810
T_s (°F)	3,640	3,670	3,710
q_s/q_o	.0420	.0425	.0432

Table 7. Comparison of Results at Three Locations in the Oxy-acetylene Facility

	U = .10	U = .181	U = .30
$\rho D_{12}\sum h_{iw}\partial Y/\partial y)_w/q_o$	.057	.158	.2061
$\rho U_w(h_w-h_s)/q_o$	.069	.0378	.0245
$\int_o^\tau q_s(\tau)\,d\tau\,/q_o\tau$	.0854	.0844	.0762
$\int_o^\tau \rho U_w \int_{T_v}^{T_s} C_{p_v}\,dT\,d\tau/q_o\tau$	.0374	.0413	.0382
$\int_o^\tau \rho U_w\,\Delta h_v\,d\tau/q_o\tau$	.0271	.0205	.0157
Time (τ) at $X_v/L = .95$	1070	810	700.3
T_s at $X_v/L = .95$ (°F)	2730	3710	4310
q_s/q_o at $X_v/L = .95$	.045	.0432	.0396
q_o (BTU/ft^2-sec)	85.1	150.0	226.9

then be expected that application of this system in an air environment at an equivalent cold-wall heating rate would result in a decrease in the net heat transfer to the surface. It is also seen that even though the cold-wall heating rate increases, the percentage of this value transmitted to the surface is lower with increasing U. The ratio E_V/E_I is calculated to be 1.38, 2.02, and 2.43 respectively for U = 0.10, 0.181, and .30. This again indicates the increasing importance of vapor specific heat as the heating rate rises.

Up to this point, the analysis of Chapter III has been applied only to environmental conditions calculated for an oxy-acetylene combustion facility. It was desired to evaluate the thermal response of the impregnated ceramic for conditions in an air environment. Two conditions were chosen for comparison, U = 0.181 and U = 0.30. For comparison purposes it was assumed in each case that the cold-wall heat flux and free stream static temperature were the same as those calculated for the respective conditions in the oxy-acetylene environment (typically, in the past, these parameters were selected for comparison purposes). The freestream enthalpy, density and composition were assumed to be that of equilibrium air at atmospheric pressure with the stagnation point velocity gradient calculated from the cold-wall heat flux. A summary of conditions for the air environments is shown in Table 8.

A comparison of results for air and C_2H_2 - air are shown in Tables 9 and 10 for U = 0.181 and U = 0.30 respectively. The results for U = 0.181 indicate less heat transfer to the porous matrix and a subsequent longer protection time for the air environment. This

Table 8. Environmental and Boundary Conditions for Air Environment

	U = .181	U = 0.30
Te (°R)	4977	5744
q_o (BTU/ft^2 sec)	150.0	226.9
he (BTU/lbm)	1267.7	1880.9
hw (BTU/lbm)	0.0	0.0
μe (lbm/ft sec)	$4.95 \cdot 10^{-5}$	$5.35 \cdot 10^{-5}$
ρ_e (lbm/ft^3)	.0079	.0066
dU/ds (sec^{-1})	30,400	169390.0

TABLE 9. COMPARISON OF RESULTS FOR AIR AND C_2H_2-AIR AT U = 0.181 $x_v/L=.95$

	C_2H_2-Air	Air
$\rho D_{12} \sum h_{iw} \left.\frac{\partial y_i}{\partial y}\right)_w \Big/ q_o$	.1582	.0515
$\rho V)_w \; (hw-hs)/q_o$	.038	.0515
$\int_0^{\tau} q_s(\tau)\, d\tau$ (BTU/ft^2)	10,230	10,201
$\int_0^{\tau} m_v \int_{T_v}^{T_s} C_p dT d\tau$	5202	5275.1
$\int_0^{\tau} m_v \, \Delta h_v d\tau$	2494.4	2494.3
T_e (°F)	3707	3711.6
TIME (τ) (sec)	786.0	801.2
q_s/q_o	.0425	.0445

TABLE 10. COMPARISON OF RESULTS FOR AIR AND C_2H_2-AIR AT U = 0.30, X_v=95

	C_2H_2-Air	Air
$\rho D_{12} \sum hi_w \left.\frac{\partial y_i}{\partial y}\right)_w / q_o$	.2061	.0383
$\rho V\,)_w (h_w - h_s)/q_o$	.0245	.0383
$\int_o^\tau Q_s(\tau)\ d\tau$ (BTU/ft^2)	12032.8	12466.5
$\int_o^\tau m_v \int_{T_v}^{T_s} C_{p_v}\ dt d\tau$	6060.8	6288.9
$\int_o^\tau m_v \Delta h_v d\tau$	2494.4	2494.4
T_s(°F)	4310	4490
TIME (τ) (sec)	700.3	675.8
q_s/q_o	.0396	.0434

trend was expected due to the estimated reduction in the contribution of surface recombination to the heat transfer. The smaller magnitude of this term is indicated in Table 9, however, its effect was less than expected considering the small reduction in surface heat transfer. This is attributed to two effects.

It can be seen from Table 8 that the stagnation point velocity gradient is approximately twelve percent larger at the same cold-wall heating value in the C_2H_2 - air environment. From equation 3.33, this would reduce the surface injection parameter at a specified $\rho v)_w$ and thus yield less reduction in surface heat transfer due to mass injection. A comparable effect on surface element mass fraction with injection rate would also occur. A second effect was the difference in free stream and surface enthalpies for the air and C_2H_2 - air environments. The ratio of this enthalpy difference at a surface temperature of $3600^{o}F$ to the cold-wall, zero injection value is significantly higher for the air environment, 0.54 versus 0.42. Thus, at a given free stream to surface temperature difference, the "hot-wall" reduction of surface heat transfer was less for the air environment.

A comparison of results for U = 0.30 shows that the calculated heat transfer was greater for the air environment with a corresponding reduced protection time. The net surface chemistry terms from equation 5.1 was again less for the air environment. This would tend to reduce the surface heat transfer. However, both the stagnation point velocity gradient and "hot-wall" correction for the air environment equivalent to U = 0.30 had the tendency to increase surface heat flux for a given surface temperature and injection rate. It is also noticed that in each case the two surface chemistry terms of equation 5.1 are equal for the air environment. From equation 3.17, it is seen that the net contribution of surface chemistry to the heat transfer is zero for this case. This was a result of the surface temperature being lower than that necessary to cause significant dissociation of H_2O and due to the absence of free stream CO and H_2 to promote surface recombination. As for the previous cases, the contribution of the heat capacity of the impregnate vapor increases with surface temperature.

Thus, a comparison of results for C_2H_2 - air and air environments based on the same value of q_o and T_E indicates minimal difference in the total protection time. However, significant differences in the relative contribution of individual thermal protection mechanisms were observed. In general, an evaluation of effects such as environmental chemistry could best be made by an analysis of the environment in question at known boundary conditions. However, in comparing the effects of two different free stream chemistries, a comparison based on conditions other than q_o and T_E could possibly give more insight into relative chemistry effects.

CHAPTER VI

CONCLUSIONS

An analytical and experimental investigation of the thermal response of a porous, impregnated ceramic has been made and experimental tests performed in the exhaust of an oxy-acetylene combustion facility. The theoretical analysis considered the coupling effects of environment chemistry and surface injection in the prediction of surface chemistry and heat transfer. Results of the theoretical analysis were compared for C_2H_2 - air and air environments at equal values of free stream temperature and cold-wall heat flux. The relative contributions of surface chemistry, impregnate vapor heat capacity, interface vaporization and surface temperature rise to the total thermal protection was considered for all cases. The conclusions from these investigations are:

1. Element chemistry variations along the axis of a free jet occur as a result of jet mixing with the surrounding atmosphere. This appreciably alters the environmental chemistry at successive locations along the axis of an oxy-acetylene torch.

2. Even though the surrounding atmosphere is air, stoichiometric ratios of fuel to oxygen and nitrogen may not occur along the axis of the jet.

3. For environments where surface recombination is possible for CO_2 and H_2O, the free stream oxygen concentration is important in

the amount of surface recombination.

4. A comparison of experimental and theoretical results for interface recession exhibited good agreement during the initial heating period. The theoretical prediction tended to lag experimental results during the last phase of interface recession. This was possibly a result of incomplete gel impregnation near the cemented surfaces.

5. The predicted net contribution of surface chemistry to the energy transfer at the surface was to increase the net surface heat flux due to surface recombination.

6. At a cold-wall heating rate of 150 BTU/ft^{2}sec, impregnate vapor heat capacity contributes approximately 50 percent of the total thermal protection with approximately 20 percent of the protection a result of interface vaporization. For this case, vapor specific heat would be more important than effective heat of vaporization as a criteria for impregnate selection. This effect increased with an increase in surface temperature of the heated slab.

7. In comparing results for C_2H_2 - air and air environments, the lower contribution of surface recombination in the air environment was generally offset by a smaller effect of surface injection and less surface heat flux reduction due to "hot-wall" effects in the air environment.

APPENDIX A

FORMULATION OF ENERGY EQUATIONS

A control volume taken from Region I in Figure 1 is shown in Figure 25.

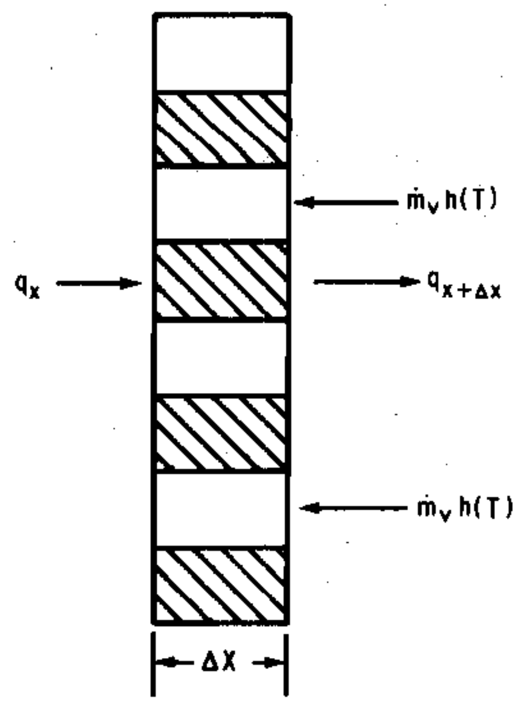

Figure 25. Energy Balance Control Volume for Region I

The following effects were considered in the control volume:

1. Heat conduction in and out
2. Convective enthalpy flux in and out

3. Transient energy storage

The heat flux and vapor flow were assumed to be one-dimensional in the direction normal to the heated surface. Distribution of the void space was assumed to be homogeneous through-out the system with a porosity of 0.60. Radiation and dissociation of impregnate vapor were neglected in the formulation of the energy equation. The impregnate vapor released at the interface was assumed to be water vapor behaving like an ideal gas. The average pore diameter of the silica foam used in this investigation was approximately two percent of the slab thickness. Thermal equilibrium was assumed to exist between the solid matrix and impregnate vapor. This was partially justified by the magnitude of flow rates predicted by the analysis of Chapter III. The calculated vapor flow rate was less than 0.006 lbm/ft^{2}sec for 90 percent of the duration of the tests.

Application of the first law of thermodynamics for a control volume with the assumptions discussed above yields equation A.1.

$$- k_1 \frac{\partial T}{\partial x}\Big)_x + k_1 \frac{\partial T}{\partial x}\Big)_{x + \Delta x} = \dot{m}_v\, h_t\big)_x \tag{A.1}$$

$$- \dot{m}_v\, h_t\big)_{x+\Delta x} + \rho_1 C_1 \frac{\partial T}{\partial \tau} \Delta x$$

Dividing by Δx and taking the limit as Δx approaches zero yields equation A.2

$$\rho_1 C_1 \frac{\partial T}{\partial \tau} = \frac{\partial}{\partial x}\left(k_1 \frac{\partial T}{\partial x}\right) + \frac{\partial}{\partial x}\left(\dot{m}_v\, h_t\right) \tag{A.2}$$

Equation A.3, representing the energy equation for Region II, was obtained in a similar manner.

$$\rho_2 C_2 \frac{\partial T}{\partial \tau} = \frac{\partial}{\partial x}\left(k_2 \frac{\partial T}{\partial x}\right) \tag{A.3}$$

Coordinates of the moving reference frame system are shown in Figure 1 and are defined by equations A.4.

$$x = x' + \int_{\tau_o}^{\tau} V_v(\tau)\, d\tau \tag{A.4}$$

$$\tau = \tau'$$

Application of the chain rule yields the following transformations:

$$\frac{\partial}{\partial x} = \frac{\partial}{\partial x'} \qquad \frac{\partial^2}{\partial x^2} = \frac{\partial^2}{\partial x'^2} \tag{A.5}$$

$$\frac{\partial}{\partial \tau} = - V_v(\tau) \frac{\partial}{\partial x'} + \frac{\partial}{\partial \tau'}$$

The result of the coordinate transformation is the appearance of the convective term, $V_v \frac{\partial}{\partial x'}$, which accounts for the movement of the slab into the control volume in the moving reference frame system. Note that it has not been necessary to assume that the interface velocity is constant or that it varies in any given manner.

Performing the indicated transformation, the energy equations become:

Region I

$$\rho_1 C_1 \frac{\partial T}{\partial \tau'} = \frac{\partial}{\partial x'} \left(k_1 \frac{\partial T}{\partial x'} \right) + \frac{\partial}{\partial x'} (\dot{m}_v h_t) \tag{A.6}$$

$$+ \rho_1 C_1 V_v \frac{\partial T}{\partial x'}$$

Region II

$$\rho_2 C_2 \frac{\partial T}{\partial \tau'} = \frac{\partial}{\partial x'}\left(k_2 \frac{\partial T}{\partial x'}\right) + \rho_2 C_2 V_v \frac{\partial T}{\partial x'} \qquad (A.7)$$

APPENDIX B

CALCULATION OF SPECIES MASS FRACTIONS

The results of this appendix present the calculation procedure required to determine species mass fractions. This analysis was used to determine both free stream and surface chemistry for the element mass fractions predicted respectively from equations 3.47b and 3.41. The local thermodynamic temperature was assumed known or assumed for the purpose of this section.

A mixture of oxygen and acetylene was burned in an air environment, and thus the elements present were oxygen, hydrogen carbon, and nitrogen. The presence of these four elements allowed four equations to be written for conservation of elements. The remaining number of equations required depends upon the number of species which were considered. The species considered were carbon dioxide, carbon monoxide, water vapor and molecular oxygen, nitrogen, and hydrogen. An evaluation of the significant equilibrium constants in the range of 5000^{o}R and below eliminated consideration of other possible species such as atomic hydrogen, oxygen, and oxides of nitrogen. Thus based on these six species, equations B.1 were solved simultaneously to determine the individual species mass fractions, Y_i. For the purpose of this analysis, subscripts 1-6 denote respectively H_2O, CO_2, O_2, CO, H_2 and N_2.

$$Y_1 + Y_2 + Y_3 + Y_4 + Y_5 + Y_6 = 1.0 \tag{B.1a}$$

Conservation of Hydrogen

$$\frac{2.016}{18.016} Y_1 + Y_5 = \bar{\bar{Y}}_H \tag{B.1b}$$

Conservation of Carbon

$$\frac{12.0}{44.} Y_2 + \frac{12.0}{28.} Y_4 = \bar{Y}_C \tag{B.1c}$$

Conservation of Nitrogen

$$Y_6 = \bar{Y}_N \tag{B.1d}$$

Equilibrium Reaction

$$CO + \tfrac{1}{2}O_2 \rightleftharpoons CO_2$$

$$\frac{Y_2}{Y_4\sqrt{Y_3}} = \frac{K_{P_1}\ P_T^{\frac{1}{2}}\ M_2\sqrt{M}}{M_4\sqrt{M_3}} \qquad \text{(B.1e)}$$

Equilibrium Reaction

$$H_2 + \tfrac{1}{2}O_2 \rightleftharpoons H_2O$$

$$\frac{Y_1}{Y_5\sqrt{Y_3}} = \frac{K_{P2}\ P_T^{\frac{1}{2}}\ M_1\sqrt{M}}{M_5\sqrt{M_3}} \qquad \text{(B.1f)}$$

At this point, it has been assumed that the gas mixture and the individual species are ideal gases (constant specific heats have not been assumed) and that the individual species are in local chemical equilibrium.

The mass fractions of molecular nitrogen can be obtained directly from equation B.1d. This leaves five equations to be solved simultaneously for the remaining mass fractions. These five equations are:

$$Y_1 + Y_2 + Y_3 + Y_4 + Y_5 = A \qquad \text{(B.2a)}$$

$$Y_1 + 9Y_5 = B1 \qquad \text{(B.2b)}$$

$$Y_2 + 1.571\ Y_4 = F \qquad \text{(B.2c)}$$

$$\frac{Y_1}{Y_4 \sqrt{Y_3}} = E \qquad \text{(B.2d)}$$

$$\frac{Y_1}{Y_5 \sqrt{Y_3}} = G \qquad \text{(B.2e)}$$

where A, B, E, F, and G in B.2 are defined by equations B.1.

After eliminating Y_1, Y_2, and Y_5 and considerable algebraic manipulation, equations B.2 were reduced to those given below.

$$W = \frac{G}{E}\left\{ \frac{F - 1.571\, Y_4}{Y_4} \right\} \tag{B.3a}$$

$$\sqrt{Y_3} = \frac{W}{G} \tag{B.3b}$$

$$Y_4 = \left\{ \frac{W + 1}{W + 9}\, B1 + F - A + Y_3 \right\} / 0.571 \tag{B.3c}$$

Values for A, B1, and F were known from local element mass fractions. E and G were obtained from species molecular weights, equilibrium constants for the local temperature, and an assumed mixture molecular weight. The unknowns in equations B.3 are Y_3, Y_4, and W. Also, due to the fact that the range of possible mass fractions are limited between zero and one, equation B.3b yields the physical limitation on Y_4 that

$$0 \le Y_4 \le F/1.571 \tag{B.4}$$

or

$$0 \le Y_4 \le \frac{3.667\ \overline{Y}_c}{1.571}$$

Equations B.3 lend themselves to a systematic trial and error procedure. In general an initial assumed value of Y_4 was either high or low. The result of each possibility, applied successively to equations B.3, is shown in Table 11. The assumption of a value of Y_4 too small leads to a calculated value too large and vice versa. An initial assumed value of Y_4 just above the lower bound was substituted into the iteration procedure described in Table 11. If the calculated value was larger than the assumed value, the assumed value was too small and the procedure then repeated for a larger assumed value. At the point where the calculated value became smaller than the assumed value, upper and lower limits were established. The procedure was then repeated starting at the lower bound and proceding in increments of 10 percent of the difference in the limits. This was repeated until the error was less than 1 percent of the lower limit.

It should be noted that even though for a particular iteration, the temperature and element mass fractions are known, the mixture molecular weight, M, was not known apriori. However, a reasonable initial estiamte was made from the result of a previous iteration

Table 11. Solution Procedure for Equations B.3

	Operation	Case I	Case II
a.	Assume Y_4	Assumed Y_4 too small	Assumed Y_4 too large
b.	From B.3a, calculate W	W too large	W too small, possibly negative
c.	From B.3b, calculate $\sqrt{Y_3}$	$\sqrt{Y_3}$ too large	$\sqrt{Y_3}$ too small possibly negative
c.	From B.3c, calculate Y_4	Y_4 too large	Y_4 too small

and a test made on the resulting solution. Differences of the order of ten percent in the value of molecular weight could be tolerated as the functional dependence in equations B.1e and B.1f is proportional to $\sqrt{M}$. The error limit used was three percent.

The solution procedure outlined above was unchanged for the case in the turbulent mixing analysis of Chapter III where the temperature was not known. For this case, element mass fractions and total enthalpy were known from equations 3.47a and 3.47b. The procedure outlined above became a part of a double trial and error solution procedure in which double iteration on the temperature and species mass fraction was necessary.

Once the solution for the species mass fraction was obtained at a given assumed temperature, the enthalpy at the assumed temperature was calculated from equation B.5, again assuming mixtures of ideal gases, and compared with the value predicted from equation 3.47a.

$$h(T) = \sum_{i=1}^{6} Y_i \, h_i(T) \tag{B.5}$$

The process was repeated until the error was less than one percent.

The values used for the respective species enthalpies were obtained from curve fits of tabulated values (48). These fits were found to be accurate within one percent over the range of temperature considered and are presented in Appendix C.

APPENDIX C

THERMODYNAMIC AND TRANSPORT PROPERTY DATA

This appendix summarizes the equations, data, and sources of thermodynamic and transport properties used in this investigation. The following subscripts are used for all constants and properties of individual species: 1 = CO_2, 2 = H_2O (v), 3 = O_2, 4 = CO, 5 = H_2, 6 = N_2.

Chemical Enthalpy

Data for each of the species listed above were curve fitted from McBride, et al. (48) for the range $300^\circ K < T < 3200^\circ K$ in the form

$$h_i(T) = 1.987\ (a_1 T + a_2\ T^2/2 + a_3\ T^3/3 \qquad \text{(C.1)}$$

$$+ a_4\ T^4/4 + a_5\ T^5/5 + a_6)$$

where h_i is in cal/gm mole and T in $^\circ K$. Coefficients for each of the species are summarized in Table 12. Equations for specific heat were obtained from the first derivative of the above results.

Table 12. Coefficients for Species Enthalpy Fit.

Species	a_1	$a_2 \cdot 10^4$	$a_3 \cdot 10^8$	$a_4 \cdot 10^{12}$	$a_5 \cdot 10^{14}$	a_6
H_2O	3.7988	2.8991	151.95	-754.21	10.949	-32044.3
CO_2	6.0002	5.5766	1.4483	.15215	$5.829E^{-5}$	-49524.6
O_2	2.8594	24.489	-154.25	479.5	-5.5107	-947.5
CO	3.0445	12.547	-30.633	-18.156	1.1285	-14250.7
H_2	3.1387	8.6357	3.8596	-137.79	2.5901	-967.8
N_2	3.6872	-8.1748	110.91	-386.06	4.5258	-1073.4

Gas Mixture Viscosity

Wilke (49) reported the mixture viscosity relationship used in this investigation and given by equation C.2.

$$\mu = \sum_{i=1}^{6} \frac{x_i \mu_i (T)}{\sum_{K=1}^{6} x_K \, \phi_{iK}} \tag{C.2}$$

where Hirschfelder, Curtiss, and Bird (50) give μ_i as

$$\mu_i = 1.79396 \cdot 10^{-6} \frac{\sqrt{M_i T(^{\circ}K)}}{\Omega_i^{(2,2)*} \, (T_i^*) \, \sigma_i^{\,2}} \text{ lbm/ft sec}^2 \tag{C.3}$$

$$T_i^* = T(^{\circ}K)/(\epsilon/K)_i \tag{C.4}$$

and

$$\phi_{i,k} = \frac{1}{\sqrt{8}} \frac{\left(1 + \frac{\sigma_K}{\sigma_i} \left(\frac{\Omega_k^{(2,2)*}}{\Omega_i^{(2,2)*}} \right)^{\frac{1}{2}} \right)^2}{\left(1 + \frac{M_i}{M_k}\right)^{\frac{1}{2}}} \tag{C.5}$$

$\Omega_i^{(2,2)*}$ (T*) = Normalized deviation of collision cross-section relative to ideal, rigid-sphere behavior.

Data for the force constants σ_i, $(\varepsilon/K)_i$, and $\Omega_i^{(2,2)*}$ were taken from reference (50) for results based on the Lennard-Jones (6-12) potential. These are summarized in Table 13.

Gas Mixture Thermal Conductivity

Mason and Saxena (51) report an approximate expression given by equation C.6 analogous to equation C.2 for the thermal conductivity of low density gas mixtures.

$$k = \sum_i \frac{x_i \; k_i(T)}{\sum_j x_j \; \phi_{i,j}} \tag{C.6}$$

The expression developed by Eucken (52) was used for individual species k_i.

$$k_i(T) = R_i \mu_i (C_{vi}/R_i + 9/4) \tag{C.7}$$

The constant volume specific heat was obtained from the equations for C_{pi} discussed previously and equation C.8.

Table 13. Constants and Equations Used in Viscosity Calculations

H_2O

$$\Omega_i^{(2,2)*} = 0.67743 - 0.9465/T^* + 25.267/T^{*2} - 66.0101/T^{*3} + 74.6389/T^{*4} - 32.4117/T^{*5}$$

Other Species

$$\Omega_i^{(2,2)*} = 0.58156 + 4.1704/T^* - 24.76/T^{*2} + 89.2402/T^{*3} - 153.086/T^{*4} + 99.46411/T^{*5}$$

	H_2O	CO_2	O_2	CO	H_2	N_2
σ_i (Å)	2.824	3.897	3.541	3.706	2.915	3.794
$(\varepsilon/\kappa)_i$ (°κ)	230.9	213.0	88.0	88.0	38.0	79.8
M_i	18.016	44.01	32.0	28.01	2.016	28.02

$$C_{pi} - C_{vi} = R_i \tag{C.8}$$

Equilibrium Constants

Equilibrium constants for the equilibrium reactions considered in this investigation were curve fitted as functions of temperature from data reported by McBride, et al. (48) in the range $300^\circ K < T < 2700^\circ K$. The maximum deviations between tabulated and calculated values are less than 3.5 percent. The resulting expressions are given by equations C.9 and C. 10.

$$\log_{10} K_{p_1} = -4.48586 + 26566.8/T \; (^\circ R) \tag{C.9}$$

$$\log_{10} K_{p_2} = -2.86379 + 23127.1/T \; (^\circ R) \tag{C.10}$$

Thermal Conductivity of Porous Silica

Walton and Poulos (53) have reported properties of slip cast fused silica as a function of temperature. Using the combination formulas given by equation 3.3, calculations were made for effective thermal conductivity of the silica foam with water vapor in the void space. The results of these calculations were curve fitted as a function of temperature to yield equation C.12.

$$k_1 = 0.2127 + .00398T^3 \text{ BTU/hr ft}^{2\,\circ}\text{F} \qquad (C.12)$$

A similar procedure for Region II, the unvaporized region, yielded effective thermal conductivities with a maximum variation of four percent. A mean value given by equation C.13 was therefore used for this region.

$$k_2 = 0.366 \text{ BTU/hr ft}^{2\,\circ}\text{F} \qquad (C.13)$$

LITERATURE CITED

1. Moskowitz, S. L., and Lombardo, S., "2750 Deg F Engine Test of a Transpiration Air-Cooled Turbine," Journal of Engineering for Power, Trans. ASME, Series A, Vol. 93, April, 1971, p. 238.

2. Weinbaum, S., and Wheeler, H. L., Jr., "Heat Transfer in Sweat-Cooled Porous Metals," Journal of Applied Physics, Vol. 20, 1949, p. 113.

3. Schneider, P. J., and Brogan, J. J., "Temperature Response of a Transpiration - Cooled Plate," ARS Journal, Vol. 32, Feb., 1962, p. 233.

4. Mendelsohn, Andrew R., "Transient Temperature of a Porous-Cooled Wall," AIAA Journal, Vol. 1, June, 1963, p. 1449.

5. Grosh, Richard J., "Transient Temperature in a Semi-Infinite, Porous Solid with Phase Change and Transpiration Effects," WADD Technical Report 60-105, January, 1960.

6. Starkman, E. S., Mizutani, Y., Sawyer, R. F., and Teixeira, D. P., "The Role of Chemistry in Gas Turbine Emissions," Journal of Engineering of Power, Vol. 93, Series A, July, 1971, p. 333.

7. Bethe, Hans A., and Adams, Mac C., "A Theory for the Ablation of Glassy Materials," Journal of the Aero/Space Sciences, Vol. 26, June, 1959, p. 321.

8. Hidalgo, Henry, "Ablation of Glassy Material Around Blunt Bodies of Revolution," ARS Journal, Vol. 30, Sept., 1960, p. 806.

9. Koh, J. C. Y., and del Casal, E. P., "Heat and Mass Transfer with Chemical Reactions for Fluid Flow Through a Porous Matrix in Re-entry Thermal Protection," The Boeing Company, D2-24103-1, Dec., 1965.

10. Poulos, N. E., Walton, J. D., and Elkins, S. R., "Fused Silica-Hydrated Cements for Thermal Protection Systems," The American Ceramic Society Bulletin, Vol. 41, Dec., 1962, p. 812.

11. Gorton, Robert L., "An Experimental Study of Ammonia as a Reactive, Transpiration Coolant," Journal of Heat Transfer, Trans. ASME, Series C, Vol. 91, Nov., 1969, p. 561.

12. Lees, L., "Convective Heat Transfer with Mass Addition and Chemical Reactions," Third AGARD Combustion and Propulsion Colloquium,

Pergamon Press, New York, 1958.

13. Penner, S. S., and Williams, F., "The Theoretical Description of Laminar, Inviscid Constant-Pressure Flames Formed from Initially Separated Reactants by a Single Rate-Controlling Reaction Step, and the Burning of Single Fuel Droplets in an Oxidizing Medium," Guggenheim Jet Propulsion Center, California Institute of Technology, Technical Report No. 19, May, 1957.

14. Fox, Herbert, and Libby, Paul A., "Helium Injection Into the Boundary Layer at an Axisymmetric Stagnation Point," Journal of the Aerospace Sciences, Vol.29 , August, 1962, p. 921.

15. Georgiev, S., Hidalgo, H., and Adams, M. C., "On Ablating Heat Shields for Satellite Recovery," AVCO-Everett Research Lab., Res. Rep. 65, July, 1959.

16. Weston, Kenneth C., "The Stagnation-Point Boundary Layer with Suction and Injection in Equilibrium Dissociating Air," NASA TN D-3889, March, 1967.

17. Weston, Kenneth C., "An Approximate Analysis of the Effects of Nitrogen Injection into the Boundary Layer on a Graphite Surface in a High-Temperature Dissociated Airflow," NASA TN D-4060, July, 1967.

18. Scala, S. M., and Gilbert, L. M., "The Sublimation of Graphite at Hypersonic Speeds," G. E. Co., MSD, TIS R64SD55, August, 1964.

19. Penner, S. S., and Libby, P. A., "Convective Laminar Heat Transfer with Combustion for a Lewis Number of Unity," Astronautica Acta, Vol. 13, Jan., 1967, p. 75.

20. Faget, Max, "Space Shuttle: A New Configuration," Astronautics and Aeronautics, Vol. 8, Jan., 1970, p. 52.

21. Bayley, F. J., and Turner, A. B., "The Transpiration Cooled Gas Turbine," Journal of Engineering for Power, Vol. 92, Series A, Oct., 1970, p. 351.

22. Schmidt, Donald L., and Schwartz, Herbert S., "Evaluation Methods for Ablative Plastics," SPE Transactions, Vol. e, Oct., 1963.

23. Cutting, John C., Fay, James A., Hogan, William T., and Moffatt, W. Craig, "Heat Transfer in Dissociated Combustion Gases," Air Research and Development Command, A FOSR-TR-59-78, July, 1959.

24. Weiner, O., "The Theory of Mixtures for Fields with Constant Currents," Akademie der Wissenschaften. Leipzig Math. - Phys. Kl. Abh and lunger, Vol. 32, p. 507, (1912).

25. Deissler, R. G., and Boegli, J. S., "An Investigation of Effective Thermal Conductivities of Powders in Various Gases," Journal of Heat Transfer, Trans. ASME, Series C, Vol. 80, Oct., 1958, p. 1417.

26. Cheng, Shui-chih, "The Prediction of the Thermal Conductivity of Heterogeneous Mixtures," Ph.D. Dissertation, Auburn University, August, 1968.

27. Harrington, W. F., and von Hippel, P. H., "Structure of Collagen and Gelatines," Advances in Protein Chemistry, Vol. 16, p. 1, 1961.

28. Glasstone, Samuel, Textbook of Physical Chemistry, Second Edition, D. Van Nostrand & Co., 1946, p. 1262.

29. Haurowitz, Felix, The Chemistry and Function of Protein, Academic Press, New York, p. 117, 1963.

30. Carslaw, H. S., and Jaeger, J. C., Conduction of Heat in Solids, Ist Ed., Oxford at the Clarendon Press, 1947.

31. Wylie, C. R., Jr., Advanced Engineering Mathematics, McGraw-Hill, New York, p. 152, 1960.

32. Walton, J. D., et al., "Design and Development of an E-M Window for Air Lift Reentry Vehicles," Interim Engineering Reports Numbers 1, 2, and 3, Georgia Institute of Technology, 1963-64.

33. Dorrance, W. H., Viscous Hypersonic Flow, McGraw-Hill Book Co., Inc., New York, 1962.

34. Schlichting, Hermann, Boundary Layer Theory, McGraw-Hill, New York, p. 191, 1960.

35. Elzy, E., and Sisson, R. M., "Tables of Similar Solutions to the Equations of Momentum, Heat and Mass Transfer in Laminar Boundary Layer Flow," Bulletin No. 40, Engineering Experiment Station, Oregon State University, February, 1967.

36. Libby, Paul A., "Theoretical Analysis of Turbulent Mixing of Reactive Gases with Application to Supersonic Combustion of Hydrogen," ARS Journal, March, 1962, p. 388.

37. Donovan, Leo F., "Similarity Solution for Turbulent Mixing Between a Jet and a Faster Moving Coaxial Stream," NASA TN D-4441, March, 1968.

38. Chriss, D. E., "An Experimental Study of the Turbulent Mixing of Subsonic Axisymmetric Gas Streams," Presented at the Fourth Annual Southeastern Seminar on Thermal Sciences, UTSI, Tullahoma, Tenn., May, 1968.

39. Willbanks, Charles E., "The Ablation of Slip-Cast Fused Silica," Ph.D. Dissertation, Georgia Institute of Technology, January, 1967.

40. American Society for Testing and Materials, Committee D-20 on Plastics, "Proposed Methods for Oxy-Acetylene Ablation Testing of Thermal Insulation Materials," October, 1964.

41. Hottel, H. C., and Hawthorne, W. R., "Third Symposium on Combustion and Flame and Explosion Phenomena", p. 254, Williams & Wilkins, Baltimore, 1949.

42. Lewis, Bernard, and von Elbe, G., Combustion, Flames, and Explosions of Gases, Academic Press, New York, p. 465, 1961.

43. Gaydon, A. G., and Wolfhard, H. G., Flames, Chapman & Hall., Ltd., London, p. 299, 1960.

44. Bartholme, E., Z. Elektrochem, 54, 1950, p. 169.

45. Snedeker, R. S., and Donaldson, C. duP., "Experiments on Free and Impinging Underexpended Jets from a Convergent Nozzle," ARAP Report No. 63, September, 1964.

46. Comfor, E. H., O'Connor, T. J., and Cass, L. A., "Heat Transfer Resulting From the Normal Impingement of a Turbulent High Temperature Jet on an Infinitely Large Flat Plate," Proceedings of the 1966 Heat Transfer and Fluid Mechanics Institute, Stanford University Press, 1966, p. 44.

47. Hopkins, Hubert L., "Contribution of Dissociation to the Thermal Protection of Transpiration Cooled Materials," Student Advanced Project Report 71-434, Auburn University, Nov., 1971.

48. McBride, B. J., Heimel, Sheldon, Ehlers, J. G., and Gordon, Sanford, "Thermodynamic Properties to 6000°K for 210 Substances Involving the First 18 Elements," NASA AP-3001, 1963.

49. Wilke, C. R., "A Viscosity Equation for Gas Mixtures," J. of Chemical Physics, Vol. 15, No. 4, p. 517, 1950.

50. Hirschfelder, J. O., Curtiss, C. F., and Bird, R. B., Molecular Theory of Gases and Liquids, John Wiley and Sons, New York, N. Y. 1965.

51. Mason, E. A. and Saxena, S. C., "Approximate Formula for the Thermal Conductivity of Gas Mixtures," Vol. 1, p. 361, 1958.

52. Eucken, A., Physic, Z, Vol. 14, p. 324, 1913.

53. Walton, J. D. and Poulos, N. E., "Slip-Cast Fused Silica," Special Report No. 43, Georgia Institute of Technology, 1964.

VITA

Jerry Russell Dunn was born August 17, 1940 in Houston, Texas. Most of his elementary and secondary education was obtained in Winnie, Texas at East Chambers elementary and high schools from which he graduated valedictorian in May, 1958. The following fall he entered Lamar State College of Technology, now Lamar University, and graduated as high scholastic athlete and high scholastic engineer in August 1962. He entered Georgia Institute of Technology in September, 1962, having been awarded the NDEA fellowship for doctoral study, and received the degree Master of Science in Mechanical Engineering in September, 1964.

He presently holds the position of Assistant Professor at Auburn University. He is a member of Pi Tau Sigma, Tau Beta Pi, and the Society of Sigma Xi.

He is married to the former Sandra Caron Harrington and they have four children, three daughters and one son.